

Pyrene-acceptor molecules as fluorescence probes in phospholipid bilayers

Diplomarbeit

Humboldt-Universität zu Berlin
Mathematisch-Naturwissenschaftliche Fakultät I
Institut für Physik

Marko Förstel
geb. am 25.05.1980 in Zittau

Abstract

The photophysical behaviour of a set of four novel pyrene-acceptor fluorescence probes was investigated in a variety of environments: in solvents of different polarity, in protic solvents, in phosphocholine vesicles and on supported planar lipid layers, by means of UV/Vis absorption spectroscopy and steady-state and time-resolved fluorescence spectroscopy. The probes have a strong charge transfer character after photoexcitation. Using solvatochromic shifts, the excited state dipole moments of the probes were calculated to be appr. 21 D. Fluorescence decay times and quantum yields were used to calculate the radiative and non-radiative rate constants and the fluorescence transition dipole moments in solvents of different polarity. Strong quenching effects of protic solvents on the probes were observed. The structural differences between the probes were found to only slightly influence the excited state relaxations in homogeneous solvents. The radiative and non-radiative rate constants of the probes and the solvent relaxation times, obtained with spectral reconstruction, were used to gain information about the position of the probes in a DPPC-bilayer. First steps were made to allow a preferential orientation of the immobilised probes on glass supports.

Abstract

Es wurde das photophysikalische Verhalten von vier neuen Pyrene-Akzeptor Fluoreszenzsonden in homogenen Lösungsmitteln unterschiedlicher Polarität, in protischen Lösungsmitteln, in Phosphocholin-Vesikeln und in planaren Lipid-Schichten auf Glasträgern mittels UV/Vis Absorptions- und stationärer und zeitaufgelöster Fluoreszenzspektroskopie untersucht. Die photoangeregten Sonden zeigen einen starken Charge-Transfer Charakter. Mit Hilfe der solvatochromen Verschiebungen der Fluoreszenzmaxima der Sonden in Lösungsmitteln unterschiedlicher Polarität wurden die Dipolmomente der angeregten Zustände zu ca. 21 D berechnet. Starke Fluoreszenzlöschungseffekte durch protische Lösungsmittel wurden beobachtet. Die strukturellen Unterschiede der Moleküle haben nur geringen Einfluss auf das Relaxationsverhalten in homogener Lösungsmittelumgebung. Die Geschwindigkeitskonstanten für den Fluoreszenzzerfall und die strahlungslosen Zerfälle sowie Lösungsmittelrelaxationszeiten, die durch die Methode der spektralen Rekonstruktion bestimmt wurden, wurden angewendet, um Informationen über die Position der Moleküle in einer DPPC-Doppelschicht zu erhalten. Erste Experimente wurden durchgeführt, um eine Vorzugsorientierung der immobilisierten Sonden auf Glasträgern zu realisieren.

Danksagung

An dieser Stelle möchte ich mich herzlichst bei all denen bedanken, die zum Entstehen dieser Arbeit beigetragen haben.

Herrn Prof. Wolfgang Rettig und Frau Prof. Beate Röder für die Betreuung der Arbeit.

Dr Willi Weigel gebührt Dank für stundenlange Diskussionen und unheimliche Geduld. Vielen Dank, es war eine Freude mit Dir zu arbeiten... und natürlich mit der Arbeitsgruppe von Prof. Rettig, Lars, Aniko, Gül, Hani und Anette.

Dr. Lars Dähne von der Capsulation Ag und Prof. Gradzielski und Jens Popig von der TU-Berlin für Equipment und Unterstützung bei den DLS Messungen.

Prof. Klaus Rademann für die Bereitstellung der AFM Apparatur.

Dr. Dirk Schubert von der ETH-Zürich für die Synthese von PA3b. Dr. Julia Bricks von der Akademie der Wissenschaften in Kiew gebührt besonderer Dank für die aufopferungsvolle Synthese von PA3, PA5 und PA11.

Bei der Entwicklung der Probenhalter wäre ich ohne die Unterstützung von Bernd Lück und seinen Technikern nicht sehr weit gekommen.

Jens, Martin, Olli, Nico und Christian hatten immer gute Ratschläge parat. Die schlagkräftige Unterstützung vom YelloV e.V. hätte ich auch nicht missen wollen.

Meiner Familie danke ich dafür, dass sie mich in Allem unterstützt und mitfiebert hat.

Nicht genug danken kann ich Leslie Kuo. Amicus certus in re incerta cernitur.

Abbreviations

CT	charge transfer
ET	electron transfer
FC	Franck Condon
LE	locally excited
TICT	twisted intramolecular charge transfer
MICT	mesomeric intramolecular charge transfer
S_0	singlet ground state
S_1, S_2	first and second electronically excited state
IC	internal conversion
ISC	intersystem crossing
D	molecular moiety acting as electron donor
A	molecular moiety acting as electron acceptor
D-A	composite molecule consisting of a donor and acceptor moiety linked by a single bond
UV/Vis	ultraviolet and visible
TC-SPC	time-correlated single photon counting
SR	spectral reconstruction
TRES	time-resolved emission spectra
FWHM	full width at half maximum
TAC	time to amplitude converter
MCA	multi channel analyzer
ADC	amplitude to digital converter
CFD	constant fraction discriminator
PMT	photomultiplier tube
MCP-PMT	microchannel plate photomultiplier tube
AFM	atomic force microscopy
ACN	acetonitrile
BCN	butyronitril
EtOH	ethanol
DE	diethyl ether
THF	tetrahydrofuran

DPPC	1,2-dipalmitoyl-sn-glycero-3-phosphocholine
DMABN	dimethylaminobenzonitrile
PhP	1-phenylpyrene
PA0	Dimethyl 2-(pyren-1-yl)benzene-1,4-dioate
PA3	ammonium salt of dimethyl 2-(3-aminopropyl)-5-(pyren-6-yl)benzene-1,4-dioate
PA5	ammonium salt of dimethyl 2-(5-aminopentyl)-5-(pyren-6-yl)benzene-1,4-dioate
PA11	ammonium salt of dimethyl 2-(11-aminoundecyl)-5-(pyren-6-yl)benzene-1,4-dioate
PA3b	ammonium salt of 1,4-benzenedicarboxylic acid,2-(3-aminopropyl)-5-(1-pyrenyl)-,bis[3-[2,5-bis(methoxycarbonyl)-4-(4,5,9,10-tetrahydro-1-pyrenyl)phenyl]propyl]ester
2AS	2-(9-anthroyloxy)stearic acid
6AS	6-(9-anthroyloxy)stearic acid
9AS	9-(9-anthroyloxy)stearic acid
12AS	12-(9-anthroyloxy)stearic acid
16AP	16-(9-anthroyloxy)palmitoic acid
PMA	pyrenemethylamine
Rho110	rhodamine 110
TRIS-HCl	2-amino-2-(hydroxymethyl)-1,3-propanediol, hydrochloride
SUV	small unilamellar vesicles
LUV	large unilamellar vesicles

Contents

2	Introduction	1
3	Theoretical principles and methods	3
3.1	Fluorescence spectroscopy	3
3.1.1	Charge transfer in excited states and conformational relaxation	4
3.1.2	Quenching of fluorescence	6
3.2	Time-domain lifetime measurements	8
3.2.1	Fluorescence decay time	8
3.2.2	Time-correlated single-photon counting	9
3.2.3	Data analysis	12
3.3	Solvent relaxation	13
3.4	Lipid bilayers	20
3.4.1	Lipids	20
3.4.2	Fluorescence probes in lipid bilayers	23
4	Results and discussion	27
4.1	Pyrene-acceptor probes in homogeneous solvent environments	27
4.1.1	UV/Vis absorption and fluorescence spectra	27
4.1.2	Fluorescence quantum yields and decay times	34
4.1.3	Quenching effects of protic solvents	35
4.2	Pyrene-acceptor probes in phospholipid bilayers	41
4.2.1	Vesicle preparation and characterisation	41
4.2.2	UV/Vis absorption and fluorescence spectra of pyrene-acceptor probes in DPPC-vesicles	43
4.2.3	Fluorescence quantum yields and decay times of the probes in DPPC-vesicles	45
4.2.4	Temperature effects	46
4.3	Solvent relaxation	46
4.3.1	Spectral reconstruction	47
4.3.2	Time-zero estimation	51
4.3.3	Time-resolved full width at half maximum	52
4.3.4	Spectral response function	54

4.4	Dye immobilisation and supported bilayers	56
4.4.1	Immobilised fluorophores on a glass support	56
4.4.2	Supported DPPC-layers on blank and C ₁₂ coated glass slides	58
5	Experimental Part	63
5.1	Synthesis of the probes	63
5.2	UV/Vis absorption and fluorescence measurements	63
5.3	TC-SPC	64
5.4	Vesicle preparation	64
5.5	Dynamic light scattering	64
5.6	Glass slide preparation	65
5.7	Contact angle measurements	65
5.8	Atomic force microscopy	66
5.9	Vesicle fusion	66
6	Summary	67

Chapter 2

Introduction

Charge transfer and electron transfer systems have long been under intensive study. Electric fields in the form of localised charges in proteins are also of great interest; for example, they are thought to influence the photophysics of retinal, the light absorbing molecule in the eye and thus allow us to see in color [1].

When a molecule absorbs a photon of a certain energy, its electron distribution changes and a photoexcited molecule with different physical properties results, which can interact with its environment in a different way than the molecule in its ground state. Electrical fields affect the electron distribution in the initial molecule as well as in the excited molecule. For example, the UV/Vis absorption and fluorescence spectra of fluorophores in solution can differ in solvents of different polarity, which can be explained by describing the effects of solvent polarity in terms of an electric field influencing the fluorophores' electron distribution.

A charge transfer system involves an electron donor and an electron acceptor, which may be two distinct parts of a single molecule. Upon photoexcitation, an excited charge transfer state with a high dipole moment is formed. In the case of the transfer of a full electron, this process is called "electron transfer", whereas the more general term "charge transfer" also includes systems in which only a partial charge separation takes place. An electric field applied parallel to the dipole moment in a charge transfer system can significantly influence the charge transfer process and thus allows the study of the charge transfer process in more detail than is possible in homogeneous solvent environments [2–5].

This work will lay the foundation for studying oriented charge transfer systems under the influence of an applied electric field of defined magnitude and orientation.

For this purpose, four novel fluorescence probes were synthesised. Their

photophysical behaviour will be characterised using UV/Vis absorption and steady-state and time-resolved fluorescence spectroscopy. The fluorescence probes are pyrene-acceptor derivatives, where pyrene acts as the donor and dibenzoate as the acceptor. In addition each probe has an alkyl chain with an ionic headgroup, which allow incorporation into self-organising lipid bilayers with a preferential orientation of the donor-acceptor system parallel to the bilayer normal.

In the first part of this work, the photophysics of the four probes will be studied in homogeneous solvents of different polarity and in protic solvents, in order to characterise the photophysical processes that the molecules undergo upon photoexcitation and to show that the structural differences of the molecules do not significantly affect their charge transfer character and their photophysics. The characterisation of the photophysical processes which the probes undergo upon photoexcitation in homogeneous solvents is necessary to interpret the processes in more complex environments.

In the second part of this work, the probes will be incorporated into lipid bilayers in the form of vesicles. The photophysical behaviour of the probes will be studied. Solvent relaxation times will be calculated using the method of spectral reconstruction. The positions of the probes in a lipid bilayer will be characterised using the results from the first and second part.

In the third part of this work, experimental steps toward providing immobilised and preferentially oriented donor-acceptor probes on glass surfaces will be made. Hydrophilic glass surfaces will serve as support for lipid bilayers and functionalised hydrophobic slides as a support for lipid monolayers.

Chapter 3

Theoretical principles and methods

3.1 Fluorescence spectroscopy

S_0 denotes the electronic ground state of a molecule. If the molecule absorbs light of a certain wavelength it will be promoted to an electronically excited state $S_{n>0}$. Following Kasha's rule, radiative processes occur from the S_1 state, independent of the energy of the electric state excited initially. To reach the stable S_0 state again, the molecule has several pathways to release the energy stored as the difference between the potential energy of the S_1 and S_0 states. These pathways include the radiative pathway: emitting a photon (fluorescence), and the non-radiative pathways: internal conversion (IC), intersystem crossing (ISC), charge transfer (CT) and quenching. These processes, in competition with each other, depopulate the excited state. The emissive rate, or the reciprocal observed fluorescence lifetime of a fluorophore, $1/\tau$, is therefore the sum of the intrinsic fluorescence rate constant k_f and the sum of the non-radiative rate constants k_{nr} :

$$\frac{1}{\tau} = k_f + k_{nr} \quad (3.1)$$

The quantum yield Φ_f is the ratio of the number of photons emitted by the fluorophore to the number of photons absorbed:

$$\Phi_f = \frac{k_f}{k_f + k_{nr}} \quad (3.2)$$

The measurement of τ and Φ_f thus allows the calculation of the radiative and non-radiative rate constants:

$$k_f = \frac{\Phi_f}{\tau} \quad (3.3)$$

$$k_{nr} = \frac{1 - \Phi_f}{\tau} \quad (3.4)$$

The measurement of τ will be explained in Section 3.2. Φ_f can easily be obtained with a reference dye of known quantum yield using:

$$\Phi_f = \Phi_{st} \left(\frac{I_f}{I_{st}} \right) \left(\frac{n_f^2}{n_{st}^2} \right) \quad (3.5)$$

I denotes the integrated emission spectra and n the refractive index of the solvent. The subscripts f and st denote the measured probe and the standard dye, respectively.

3.1.1 Charge transfer in excited states and conformational relaxation

The change in the electronic state of a molecule involves the motion of an electron from one orbital to another. If the final and the initial orbital of the electron are separated in space then the dipole moment will change. If this change is large, the excited state is called the charge transfer (CT) state. The excited state dipole moment of a fluorophore can be calculated by measuring the Stokes-shift, which is an effect of solvent relaxation, (Section 3.3). A CT state requires two distinguishable parts of a molecule. One acts as the electron donor, the other as the electron acceptor. A criterion for whether a charge transfer is thermodynamically allowed is given by the Rehm-Weller equation [6, 7]:

$$\Delta G = E_{1/2}^{Ox}(D) - E_{1/2}^{Red}(A) - E^* \quad (3.6)$$

where ΔG , the free enthalpy, is the driving force of the formation of a charge transfer system. $E_{1/2}^{Ox}(D)$ is the oxidation potential of the donor and $E_{1/2}^{Red}(A)$ is the reduction potential of the acceptor. E^* is the energy of the absorbed photon. A value of $\Delta G < 0$ thermodynamically allows the formation of a photoexcited CT state.

The photophysics of CT systems can also be highly influenced by the conformational dynamics [8, 9] of the donor and acceptor pair upon photoexcitation. For example the charge transfer in dimethylaminobenzonitrile (DMABN) has been studied extensively [9–12]. In the ground state, DMABN is planar and thus the conjugation between the NMe_2 group and the aromatic ring is at a maximum. After photoexcitation, DMABN is transferred into its planar excited LE state. Another excited state of DMABN also exists, in which the NMe_2 group and the aromatic ring are twisted at right angles to one another and the conjugation between the two groups is completely lost. This twisted intramolecular charge transfer (TICT) state has a high dipole moment and thus solvents of high polarity stabilise the TICT state at a lower energy level than that of the LE state. This model can explain why DMABN shows dual fluorescence in solvents of high polarity.

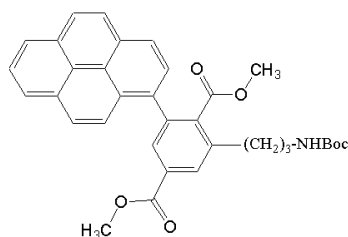


Figure 3.1: 2,5E-PP. After [13].

Internal conformational changes of a donor-acceptor system with flexible single bonds between the donor and acceptor can occur in two directions. Molecules in the form $D - \pi - A$, in which the donor and acceptor are connected to a conjugated system, may not be planar in the ground state. Upon photoexcitation, the dihedral angle between the donor and acceptor may increase, weakening the conjugation (TICT), or the angle can decrease toward a more planar conformation, increasing the conjugation. The second case has been called the mesomeric intramolecular charge transfer state (MICT) [13].

A criterion for distinguishing between the LE, TICT and MICT states is the value of the fluorescence transition dipole moment M_f in dependence on solvent polarity. It describes the fluorescent transition probability and is correlated to the radiative rate constant k_f [14–16]:

$$M_f^2 = \frac{3h}{64\pi^4 n^3 \nu_f^3} k_f \quad (3.7)$$

where M_f is the fluorescent transition dipole moment, h is Planck's constant, n is the refractive index of the solvent and ν is the emission maximum in cm^{-1} . When no conformational changes occur, M_f should be constant. When conformational changes take place and influence the conjugation between donor and acceptor, M_f is expected to decrease with decreasing conjugation and increase with increasing conjugation. For systems without conjugation (donor and acceptor at right angles), M_f is expected to be close to zero.

A CT system based on pyrene and closely related to the probes used in this work is 2,5E-PP (Figure 3.1). In [13] the photophysics of 2,5E-PP are investigated. AM1 calculations led to the conclusion, that in the ground state, the pyrene moiety is twisted by 64° to the phenyl moiety. A high excited-state dipole moment μ^* of 21.5 Debye was found, which is characteristic for a CT state. It was also found that even in non-polar solvents such as methylcyclohexane the fluorescence occurs mainly from a CT state. As solvent polarity increases the M_f value decreases, implying that increased twisting is weakening the conjugation.

3.1.2 Quenching of fluorescence

Quenching of fluorescence is any process which decreases the fluorescence intensity of a sample. Many processes are known to decrease fluorescence, for example collision or formation of complexes, and many different substances are known to act as quenchers, including oxygen, cobalt, copper, ethers and peroxides. There are two kinds of quenching: static quenching, which occurs through the formation of a complex of the fluorophore and the quencher before photoexcitation; and dynamic quenching, which occurs when a quencher comes into contact with an excited fluorophore.

A quantitative tool for describing dynamic quenching is the Stern-Volmer equation:

$$\frac{F_0}{F} = 1 + k_q \tau_0 [Q] = 1 + K [Q] \quad (3.8)$$

where F_0 and F are the fluorescence intensities in the absence and presence of a quencher with the concentration $[Q]$, τ_0 is the lifetime of the fluorophore in the absence of a quencher, k_q is the bimolecular quenching constant and K is the Stern-Volmer quenching constant. The Stern-Volmer equation can be derived using the fluorescence intensities in the presence and absence of a quencher. Under constant illumination the concentration of excited fluorophores does not change:

$$\frac{d[F^*]}{dt} = 0 = f(t) - (k_f + k_{nr}) [F^*]_0 \quad (3.9)$$

where $f(t)$ describes the constant illumination function and k_f and k_{nr} are the radiative and non-radiative rate constant, respectively. When a quencher and thus another relaxation path k_q dependent on the concentration of the quencher $[Q]$ is added, 3.9 becomes:

$$\frac{d[F^*]}{dt} = 0 = f(t) - (k_f + k_{nr} + k_q [Q]) [F^*] \quad (3.10)$$

Division of equations 3.9 and 3.10 leads to the Stern-Volmer equation: 3.8. Considering the lifetimes τ (quencher present) and τ_0 (quencher absent) which are given by:

$$\tau_0 = \frac{1}{k_f + k_{nr}} \quad (3.11)$$

$$\tau = \frac{1}{k_f + k_{nr} + k_q [Q]} \quad (3.12)$$

one obtains by division of τ_0 and τ :

$$\frac{\tau_0}{\tau} = 1 + k_q \tau_0 [Q] \quad (3.13)$$

Comparison with 3.8 shows:

$$\frac{F_0}{F} = \frac{\tau_0}{\tau} \quad (3.14)$$

The dependence of τ on the quencher concentration can only be seen in dynamic quenching, in which case the quenching acts as one of the decay processes, which depopulate the excited state. In static quenching, the lifetime shows no dependence on the quencher concentration. In this case fluorescence only occurs from the unquenched and therefore unaffected fluorophores. The theories of static quenching and of combined static and dynamic quenching can be found in detail in [17].

In the case that a fraction of fluorophores is not accessible by a quencher, a modified form of the Stern-Volmer equation can be used to obtain quantitative information about quenching efficiency. For example, this is the case when fluorophores are incorporated in lipid bilayers and a quencher cannot enter the bilayer or is embedded in the hydrophobic part of the bilayer. Considering two populations of fluorophores, one accessible by the quencher, a , and one not accessible, b , the total fluorescence is given by:

$$F_0 = F_{0a} + F_{0b} \quad (3.15)$$

where 0 refers to the intensity in absence of the quencher. In the presence of a quencher only the accessible population is quenched. Therefore the total fluorescence intensity is given by:

$$F = \frac{F_{0a}}{1 + K [Q]} + F_{0b} \quad (3.16)$$

Subtraction of Equations 3.15 and 3.16 yields:

$$\Delta F = F_0 - F = F_{0a} \left(\frac{K [Q]}{1 + K [Q]} \right) \quad (3.17)$$

Inversion of 3.17 and division into 3.15 yields:

$$\frac{F_0}{\Delta F} = \frac{1}{f_a K [Q]} + \frac{1}{f_a} \quad (3.18)$$

where f_a is the fraction of the initial fluorescence accessible to the quencher:

$$f_a = \frac{F_{0a}}{F_{0b} + F_{0a}} \quad (3.19)$$

Thus a plot of $F_0/\Delta F$ vs. $1/[Q]$ allows the calculation of K as a measurement of the quenching efficiency and of f_a as the reciprocal percentage of the fluorophores accessible to the quencher. This method has been used, for example, by Thulborne and Sawyer [18] to examine the position of different fluorophores in a lipid bilayer.

3.2 Time-domain lifetime measurements

In the last section, the fluorescence decay time τ was used to calculate the rate constants and thus to draw conclusions about conformational changes in fluorophores. Fluorescence decay times are also a useful tool to distinguish between dynamic and static quenching. This section will describe how fluorescence lifetimes can be measured and will introduce the method of time-correlated single photon counting (TC-SPC).

3.2.1 Fluorescence decay time

When a number (n_0) of fluorophores are excited at a given time $t = 0$, the excited-state population decays according to:

$$\frac{dn(t)}{dt} = -(k_f + k_{nr})n(t) \quad (3.20)$$

where k_f and k_{nr} are the radiative and the non-radiative rate constants, respectively, and $n(t)$ is the number of excited fluorophores at the time t following excitation [17]. Because emission is a statistical decay process, $n(t)$ follows an exponential decay:

$$n(t) = n_0 \exp(-t/\tau) \quad (3.21)$$

Inserting 3.21 into 3.20 and integrating on both sides yields:

$$n(t) = n_0 \exp[-(k_f + k_{nr})t] \quad (3.22)$$

where the lifetime τ is given as:

$$\tau = \frac{1}{k_f + k_{nr}} \quad (3.23)$$

In a fluorescence measurement, one usually measures the intensity $I(t)$. $I(t)$ is proportional to the number of photons $n(t)$. Therefore equation 3.22 can be written as:

$$I(t) = I_0 \exp(-t/\tau) \quad (3.24)$$

One can also define the lifetime as the average time an excited fluorophore remains in its excited state. The average time $\langle t \rangle$ can be calculated by averaging t over the intensity decay of the fluorophore:

$$\langle t \rangle = \frac{\int_0^\infty t \exp(-t/\tau) dt}{\int_0^\infty I(t) dt} \quad (3.25)$$

In a mono exponential decay, one can see easily that $\langle t \rangle = \tau$. In a multi exponential decay model, the intensity is given by:

$$I(t) = \sum_{i=1}^{\infty} I_{0i} \exp(-t/\tau_i) \quad (3.26)$$

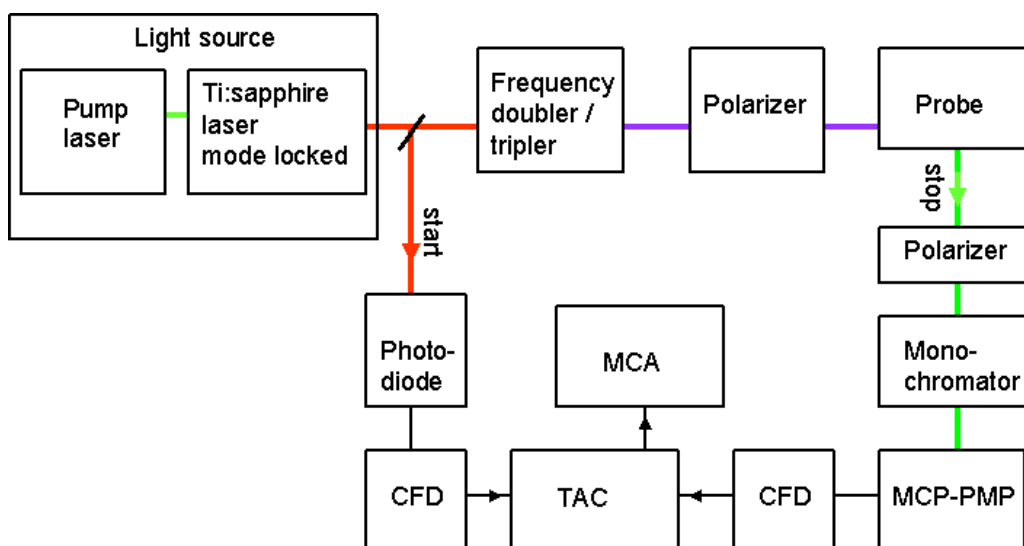


Figure 3.2: TC-SPC setup as used in our laboratory. CFD: constant fraction discriminator, TAC: time to amplitude converter, MCP-PMP: microchannel plate photomultiplier. Coloured lines describe the pathway of light. Black lines indicate a voltage signal.

where I_{0i} is the intensity of the i th component at $t = 0$ and τ_i is the lifetime of the i th component. Using equations 3.25 and 3.26, one obtains for the average lifetime $\bar{\tau}$ of a multi exponential decay:

$$\bar{\tau} = \frac{\sum_{i=1}^n I_{0i} \tau_i^2}{\sum_{i=1}^n I_{0i} \tau_i} \quad (3.27)$$

Many methods have been developed to measure the fluorescence lifetime. In the frequency-domain or phase-modulation method, the fluorophores are excited with frequency-modulated light. This causes a modulation in the emitted light, which is phase-shifted to the excitation. One can use this phase shift to calculate the lifetime. Another approach is time-correlated single photon counting, which is used in this work.

3.2.2 Time-correlated single-photon counting

Figure 3.2 shows a general setup for a TC-SPC experiment. A light source emits a pulse of light. At this moment, the time to amplitude converter (TAC) receives a start signal from a trigger (diode, photo multiplier tube (PMT), lamp control unit) through a constant fraction discriminator (CFD). The light pulse passes through a filter (monochromator, polarizer) and excites a probe. The excited probe then emits a photon which is detected by a PMT, which sends a stop signal through a CFD to the TAC. The TAC produces an output signal,

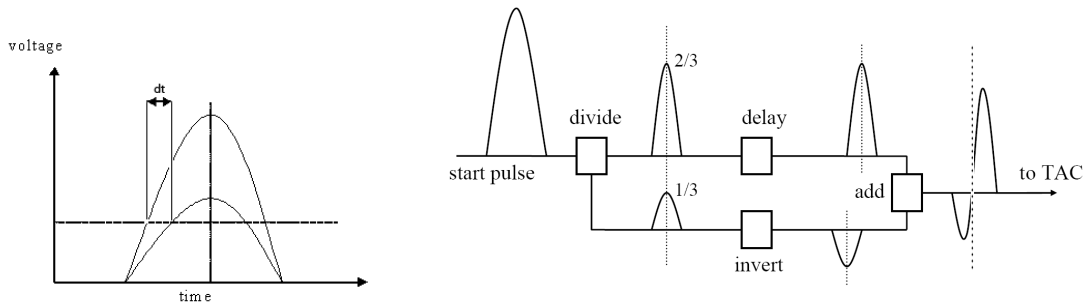


Figure 3.3: Left: Illustration of the error in a leading edge discriminator for pulses with different intensities. The dashed horizontal line marks the threshold of the discriminator. Right: principle of operation of a constant fraction discriminator. After [17].

whose voltage is proportional to the time between the start and stop signal. A multi channel analyser (MCA) uses an amplitude to digital converter (ADC) to convert this signal into a time channel and builds up a probability histogram using multiple pulse-excitation-emission cycles. The time resolution of this experiment is dependent on many factors, including the excitation pulse width and time response of the detector. In the next paragraphs, the components will be described in more detail.

Light sources

TC-SPC measurements require a light source delivering short pulses, for example a flash lamp, diode or laser, with a pulse width and pulse frequency appropriate to the decay of the probe to be observed. For example, a diode with a pulse width of around 1 ns is difficult to use for probes with decay times smaller than 1 ns. In this project, a mode-locked Ti:sapphire laser pumped by a diode solid-state laser was used. This system delivers femtosecond pulses at a frequency of approximately 81 MHz. The output wavelength can be changed using different mirror sets in the Ti:sapphire laser. To achieve wavelengths below 700 nm second and third harmonic generation was used.

Constant fraction discriminator (CFD)

A very important part of the TC-SPC setup is the CFD. It increases the time resolution of the signals from the diode and the photomultiplier in our system. The goal is to use the leading edge of the signal as the start or stop signal without losing resolution to different pulse heights.

The left side of Figure 3.3 shows how the pulse height affects the time resolution when the leading edge is used as the trigger. To circumvent this

problem, the CFD is used to split the signal in two parts, delaying one part approximately half a pulse width and inverting the other and then adds them. The obtained zero crossing point, independent of the pulse height, can be used as the trigger signal. The right side of Figure 3.3 shows this principle. CFDs can reach a resolution of approximately 30 ps.

Time to amplitude converter (TAC)

The TAC is analogous to a stopwatch, measuring the time between the arriving start and stop signals. In reaction to an incoming start pulse, the TAC charges a capacitor until either a stop pulse arrives or a set time elapses. If, for example, a time window of 20 ns is chosen, the capacitor will be fully charged at 20 ns. If a stop signal arrives after 5 ns, the capacitor will be charged to one fourth of the maximum voltage. The voltage is then read out by the multi-channel analyser (MCA). Because the TAC needs to discharge after every cycle and the discharging takes around several microseconds, it is usually run in reverse mode, meaning that the start pulse comes from a detected photon and the stop pulse from the lamp trigger. Since only one photon in approximately 100 pulses is counted, there is enough time for the TAC to discharge. An important characteristic of the TAC is its linearity. One can easily confirm the linearity by measuring light from a constant light source not dependent on the pulse. Thus, in reverse mode, the start pulses should be randomly distributed to the stop pulses (pulsed light), thus producing a constant line in the MCA.

Multi channel analyser (MCA)

The voltage, which is produced by the TAC and linearly dependent on the time between the start and stop signal, is read out by the MCA. A histogram of the number of counts in a certain voltage range is produced. The MCA used in our laboratory has 4096 channels, so for a time window of 15 ns, for example, each channel represents 3.7 ps. The produced histogram can then be read out and represents the intensity decay of the fluorophore.

Microchannel plate photomultiplier tube (MCP-PMT)

The pulse width delivered by the detector in a TC-SPC measurement is an important factor for the time resolution of the experiment. Standard photomultiplier tubes using dynodes to amplify the the signal coming from a photon have a minimum pulse width of around 0.5 ns [17]. MCP-PMT use narrow channels (4 - 12 μm) which gives a much narrower distribution of the transit times (TTS) in comparison to a dynode PMT. The MCP-PMT used in our laboratory has a TTS of around 30 ps.

3.2.3 Data analysis

The intensity decay $N(t)$ recorded using the method described above is a convolution of the so-called instrument response function or lamp function $R(t)$ with the impulse response function $I(t)$. $I(t)$ is a theoretical function which is obtained with a δ -function excitation and contains the desired "true" lifetime. When each δ -function is assumed to excite an impulse response function $I(t)$ at a given time t_k , then:

$$I_k(t) = R(t_k)I(t - t_k)\Delta t(t > t_k) \quad (3.28)$$

Here the impulse response is started at $t = t_k$. Now the measured decay $N(t)$ can be expressed as the sum of all impulse response functions:

$$N(t_k) = \sum_{t=0}^{t=t_k} I_k(t) = \sum_{t=0}^{t=t_k} R(t_k)I(t - t_k)\Delta k \quad (3.29)$$

For small Δt this can be expressed as an integral:

$$N(t) = \int_0^t R(t')I(t - t')dt' \quad (3.30)$$

$R(t)$ can be measured using a stray solution. $N(t)$ is the directly measured decay. To obtain $I(t)$, a least-square analysis can be used. Here the parameters which describe the decay $I(t)$ are iteratively aligned until the best match between the measured decay $N(t_k)$ and the computed decay $N_c(t_k)$ is obtained by minimizing the fit parameter χ^2 :

$$\chi^2 = \sum_{k=1}^n \frac{1}{\sigma_k^2} [N(t_k) - N_c(t_k)]^2 = \sum_{k=1}^n \frac{[N(t_k) - N_c(t_k)]^2}{N(t_k)} \quad (3.31)$$

where $\sigma_k = [N(t_k)]^{1/2}$ is the standard deviation following Poisson statistics and n denotes the number of channels. To interpret the quality of the fit one can use the reduced χ^2 :

$$\chi_R^2 = \frac{X^2}{n - p} \quad (3.32)$$

where n is again the number of channels and p the number of parameters used to describe $I(t)$. Depending on the model for $I(t)$, for example 3.24 or 3.26, the number of parameters can differ. χ^2 should be close to unity for each data point. The number of data points should be much higher than the number of parameters. Therefore a value of χ_R^2 close to unity indicates a good fit. Another way to characterise the goodness of a fit is a visual examination of the residuals: the differences between the calculated decay and the measured data points. A narrow, structureless distribution of the residuals around zero indicates a good fit. In this work, the decays have been fitted using 3.26 with $i \leq 3$.

3.3 Solvent relaxation

The photophysics and photokinetics of molecules are strongly influenced by their environment. These influences can be used to characterise the molecules and vice versa: well-characterised molecules can be used as probes to study their environments.

In solution, fluorophores undergo interactions which result in different spectroscopic characteristics dependent on the different properties of the solvent. Consider, for example, a molecule in the ground state S_0 with a dipole moment μ_g different from zero. This dipole moment can affect the surrounding solvent molecules, for example, influencing the orientation of surrounding solvent molecules, which also have a dipole moment. Suppose that this molecule now moves into the first excited state S_1 by absorption of a photon. Usually the dipole moment of the excited state μ^* differs from the dipole moment of the ground state μ_g . Now the surrounding solvent molecules are no longer in equilibrium with the excited molecule. A relaxation of the solvent molecules occurs and thus a new equilibrium state with the excited state of the soluted molecule is formed. The process of the relaxation from the first excited state S_1 to the state in which the solvent molecules and the soluted excited molecule are in equilibrium, is called solvent relaxation.

Figure 3.4 shows the process schematically. The described process, which results in a red-shifted emission spectra (Stokes-shift) of a fluorophore compared to its absorption spectra, can result from many dynamic processes, including the reorientation of solvent molecules, reorientation of electrons in the solvent molecules due to a different dipole moment of the excited state of the fluorophore, and specific interactions between fluorophore and molecule such as H-bonding. In fluid solvents, the solvent relaxation process usually takes place on a shorter time scale than the fluorescence deactivation processes and thus the fluorescence occurs from a completely relaxed state. In solvents of high viscosity, the solvent relaxation process can occur on a time scale close to that of the fluorescence process and therefore the emission spectra changes in time. When the solvent viscosity increases further, the fluorescence process takes place before solvent relaxation can occur. Figure 3.5 shows a simplified diagram of this process.

The molecules examined in this work are fluorophores which undergo a large change in dipole moment between the ground state S_0 and the first excited state S_1 after photoexcitation. Therefore, solvents of high polarity have a stronger influence on the excited state of the fluorophore than solvents of lower polarity. Thus the Stokes-shift increases with increasing solvent polarity. Figure 3.6 shows the potential energy of weakly and strongly interacting solvent-fluorophore pairs. For a strong interaction, the potential curve rises more strongly than for a weak interaction, resulting in an increased energy difference between the absorbed and the emitted light.

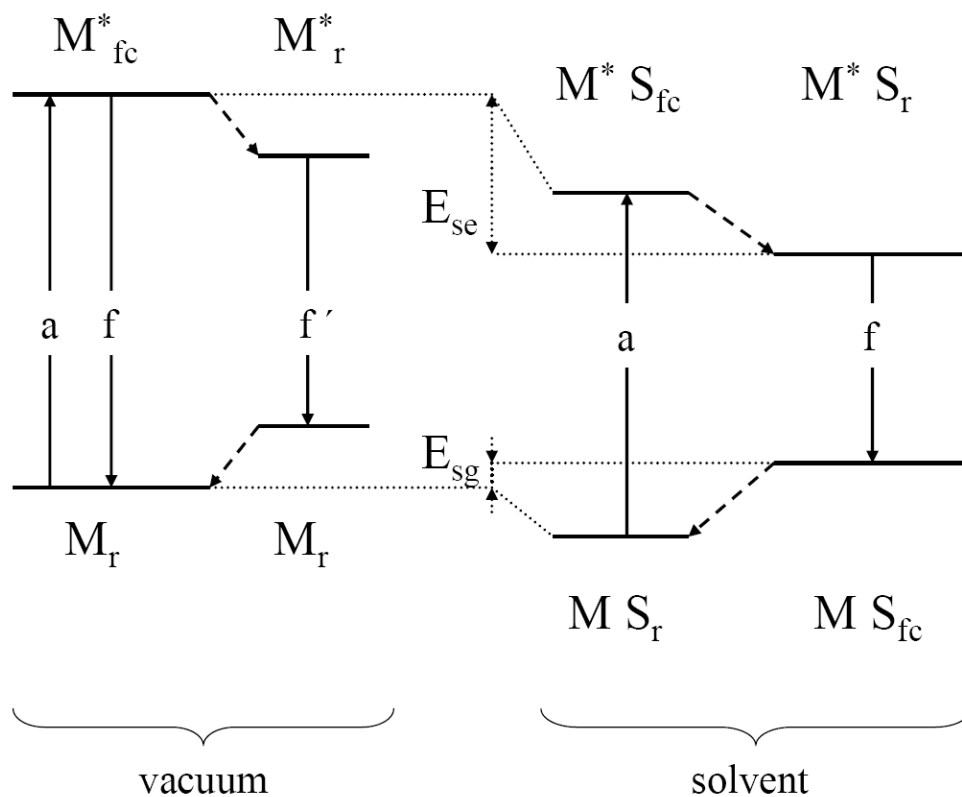


Figure 3.4: Energy diagram of the relaxation of a ground state molecule M and the excited molecule M^ in vacuum and in a solvent S . “ r ” refers to a relaxed state, “ fc ” to a Franck-Condon state; “ a ” to an absorption spectrum, “ f ” and “ f' ” to a fluorescence spectrum. E_{se} and E_{sg} indicate the energy differences in the excited and ground state, respectively. Nonradiative processes are indicated with dashed arrows, radiative processes with solid arrows. After [19].*

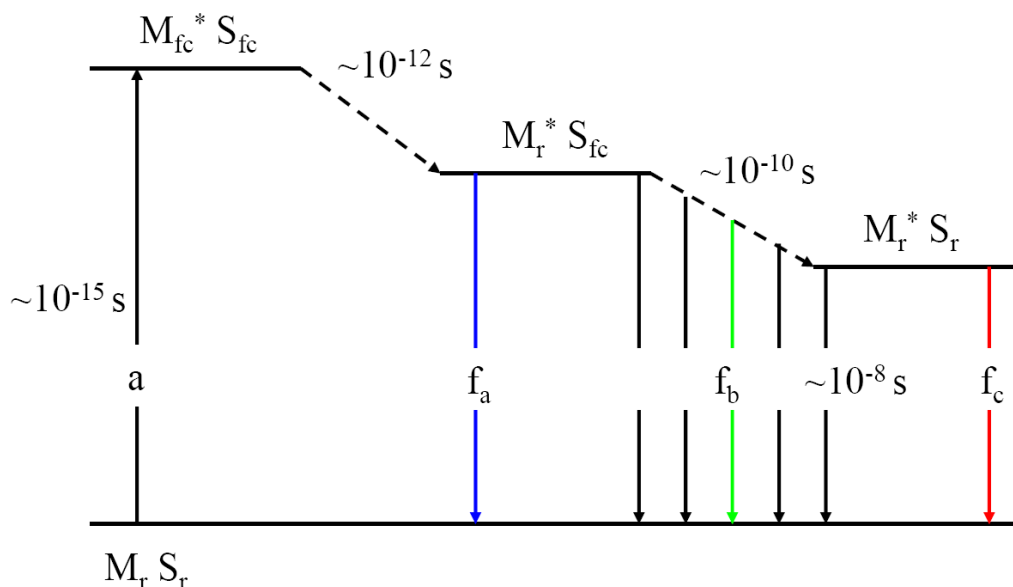


Figure 3.5: Energy diagram of the relaxation of an excited molecule M^* in solvents of different viscosity, including typical time scales. “r” refers to a relaxed state, “fc” to a Franck-Condon state, S to the solvent and “a” to the absorption process. “ f_a ” refers to a high-viscous solvent where the fluorescence process occurs before any solvent relaxation. “ f_b ” refers to a viscosity at which the solvent relaxation process is in the time scale of the fluorescence process and “ f_c ” refers to a viscosity at which the solvent relaxation process is faster than the fluorescence process. After [17].

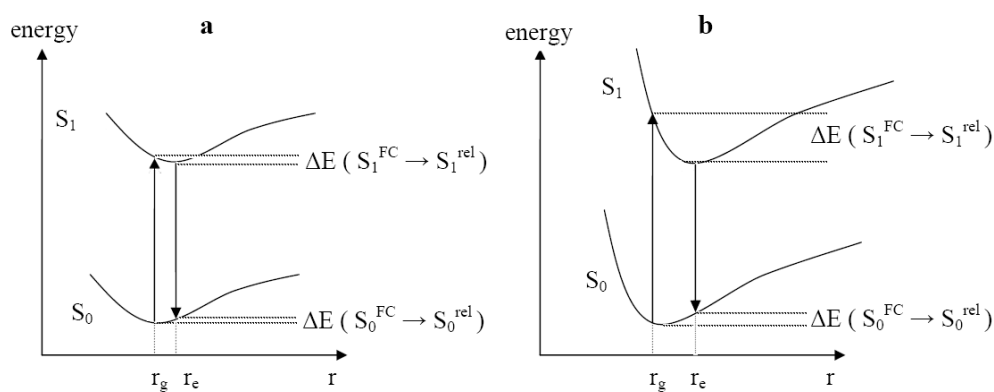


Figure 3.6: Potential energy for (a) weak and (b) strong interactions between solvent and fluorophore. The arrows pointing up marks the absorption and the arrows pointing down refer to the emission. After [17].

To obtain quantitative information about the interactions between solvents and fluorophores, the Lippert-Mataga-Equation (3.33) can be used [20–22]. This equation considers only effects of the refractive index and the dielectric constant of the solvent.

$$\Delta\nu = \nu_a - \nu_f = \frac{2(\mu^* - \mu_g)^2}{hca^3} \Delta f + \text{const.} \quad (3.33)$$

where $\Delta\nu$ is the Stokes-shift, ν_a and ν_f denote the wavenumbers in (cm^{-1}) of the maxima of absorption and emission, respectively. μ^* and μ_g refer to the excited state and the ground state dipole moment, respectively. h is Planck's constant, c the velocity of light and a refers to the solvent cavity (Onsager) radius, which is defined as the radius of a spherical cavity around the molecule in which the molecule resides. Δf describes the macroscopic polarity function:

$$\Delta f = \frac{\epsilon - 1}{2\epsilon + 1} - \frac{n^2 - 1}{2n^2 + 1} \quad (3.34)$$

where n is the refractive index, and ϵ the dielectric constant, of the solvent. The Lippert-Mataga equation also assumes that the fluorescence arises directly from the Franck-Condon state after photoexcitation. When a molecule undergoes geometrical changes after photoexcitation, for example twisting, the solvatochromic shifts of the emission can be used [22, 23] to estimate the excited state dipole moment $\mu^{*'}$. The emission maxima are now correlated to the modified $\Delta f'$ as described in equations 3.35 and 3.36,

$$\nu_f = \frac{-2\mu^{*'}(\mu^{*'} - \mu_g^{FC})}{hca^3} \Delta f' + \text{const.} \quad (3.35)$$

$$\Delta f' = \frac{\epsilon - 1}{2\epsilon + 1} - \frac{1}{2} \frac{n^2 - 1}{2n^2 + 1} \quad (3.36)$$

where μ_g^{FC} is the Franck-Condon ground state dipole moment.

The excited state dipole moment of 2,5E-PP as described in Section 3.1.1 was calculated using Equations 3.35 and 3.36 and the assumption that $\mu_g^{FC} = \mu_g$ for very small μ_g . The slope of a plot of the emission maxima over $\Delta f'$ and the knowledge of a and μ_g allows the calculation of $\mu^{*'}$. The parameter a can be obtained using the molecular density formula [24]:

$$a = \left(\frac{3M}{4\pi N_a \rho_M} \right)^{1/3} \quad (3.37)$$

A simpler approach is to take half the distance between the atoms of the molecule which provide the strongest dipole vector component [25, 26]. To obtain μ_g , semi-empirical quantum chemical procedures such as the AM1 method have frequently been used [13, 25, 26].

Dynamics of solvent relaxation

The preceding section described the influences of solvents on the emission spectra of solutes. It was mentioned that the emission spectra can change in time when the emission process takes place during the solvent relaxation process. In Figure 3.5 it is indicated under f_b that the resulting emission spectra is a composite of emission spectra from states in which the solvent is not yet completely relaxed. In this way it can be understood that an emission spectrum early in the relaxation process is blue-shifted with respect to emission spectra at later times. These spectra, representing discrete times following excitation, are called time-resolved emission spectra (TRES). The overall shift of the TRES, which is defined as:

$$\Delta\nu = \nu(t = 0) - \nu(t = \infty) \quad (3.38)$$

is proportional to the energy difference between the Franck-Condon state and the fully relaxed state of the solute. The polarity function of a solvent (Equation 3.34) was shown [27] to be directly proportional to $\Delta\nu$. Therefore the knowledge of $\Delta\nu$ can already allow conclusions about the polarity of the environment of the solute. The kinetics of the spectral shift are usually [28, 29] described using the spectral response function (correlation function) $C(t)$ which is defined as:

$$C(t) = \frac{\nu(t) - \nu(t = \infty)}{\Delta\nu} \quad (3.39)$$

Whereas the determination of $C(t)$ is the most precise way to describe the time evolution of the spectral response, the calculation of the average relaxation time:

$$\langle \tau_r \rangle = \int_{t=0}^{t=\infty} C(t) dt \quad (3.40)$$

is a simple method to obtain numerical measures of the solvation kinetics. It was shown that $\langle \tau_r \rangle$ is nearly proportional to the viscosity of the solvent [30–32]. To obtain $C(t)$ one must first obtain the TRES. The TRES have been obtained using pulse sampling and time-gated detection [33–35]. Another method which is now commonly used is the reconstruction of the TRES using wavelength-dependent decays recorded via TC-SPC. This method is described extensively by Hof et al. [28]. First, a set of fluorescence decays is recorded at several (usually 10 to 20) wavelengths of the emission spectrum. These decays are then fitted to a sum of exponentials to achieve parameterised forms $D(t, \lambda)$ of the decay curves. The TRES $S(t, \lambda)$ at any desired time are then calculated using:

$$S(\lambda, t) = \frac{D(\lambda, t)S_0(\lambda)}{\int_{t=0}^{t=\infty} D(t, \lambda) dt} \quad (3.41)$$

The TRES can then be transformed into the frequency domain and fitted. Hof et al. suggested [28] a log normal line shape function to obtain the parame-

ters full width at half maximum (FWHM), lineshape parameter and center of gravity:

$$y = a_0 \exp \left[- \frac{\ln 2 \ln \left(\frac{(x-a_1)(a_3^2-1)}{a_2 a_3} + 1 \right)^2}{\ln(a_3)^2} \right] \quad (3.42)$$

with a_0 = amplitude, a_1 = center, a_2 = width (> 0) and a_3 = shape ($> 0, \neq 1$). The time evolution of these parameters can now be used to describe the relaxation process.

Time-resolved full width at half maximum (FWHM)

Preliminary conclusions about the extent of the observed solvent relaxation process can be drawn using the time evolution of the FWHM. Experiments on lipid bilayers have shown that the FWHM should pass a maximum during the solvent relaxation process. The width of the TRES is linked to the inhomogeneity of the surrounding solvent. This can be understood when every solute is considered to have slightly different surroundings, for example, due to fluctuations of the positions of the solvent molecules. These slightly different surroundings also react slightly differently when the solute changes, for example through photoexcitation. This results in an increased inhomogeneity which decreases again when the relaxed excited state is formed and the solvent relaxation process is finished. Considering the FWHM therefore allows conclusions about the extent of the relaxation process monitored by the measurement. When only a decrease in the FWHM is observed, then parts of the solvation process are occurring faster than the time resolution of the experiment. The opposite case, an observation of only an increase of the FWHM, implies that the time window of the experiment is too short and the solvent relaxation process is not finished by the end of the measurement.

Time-Zero Estimation

To obtain the spectral response function $C(t)$ (3.39) and thus the average relaxation time $\langle \tau_r \rangle$ (3.40) it is crucial to obtain the time-zero spectra $\nu(t=0)$. $\nu(t=0)$ is a hypothetical spectrum at $t=0$, when the excited molecule is fully vibrationally relaxed (Franck-Condon state) and the solvent relaxation has not yet started. A method which obtains the position of this spectrum using only steady-state emission data, and is therefore independent of the time resolution of the experiment, has been developed by Maroncelli et al. [36] and will be outlined here. In a polar solvent, every individual solute molecule has its own local microenvironment. Assuming that every solute molecule's absorption spectrum has the same line shape function and is only shifted by a site-dependent shift δ , then the inhomogeneously broadened absorption spectrum is given by:

$$A_p(\nu) \propto \int g(\nu - \delta)p(\delta)d\delta \quad (3.43)$$

$p(\delta)$ describes here the distribution of shifts, and thus sites of the solute. The emission spectrum is considered to be the convolution of the absorption spectrum initially transferred to the excited state $g(\nu_{ex} - \delta)p(\delta)$ with the fluorescence intensity function $f(\nu - \delta)k_r(\delta)$ where ν_{ex} is the monochromatic excitation frequency and can thus be expressed as:

$$F_P(\nu, t = 0; \nu_{ex}) \propto \nu^3 \nu_{ex} \int g(\nu_{ex} - \delta)p(\delta)f(\nu - \delta)k_r(\delta)d\delta \quad (3.44)$$

k_r here refers to the radiative rate constant which is known to vary with δ . To calculate $F_P(\nu, t = 0; \nu_{ex})$, the functions $g(\nu)$, $f(\nu)$, $p(\delta)$ and $k_r(\delta)$ are required. It is further assumed that the lineshape functions $g(\nu)$ and $f(\nu)$ can be obtained from the absorption spectrum A_{np} and steady-state emission spectrum F_{np} measured in a non-polar solvent:

$$g(\nu) \propto \nu^{-1} A_{np}(\nu) \quad (3.45)$$

and

$$f(\nu) \propto \nu^{-3} F_{np}(\nu) \quad (3.46)$$

A simple assumption for the radiative rate function $k_r(\delta)$ is made using:

$$k_r(\delta) \propto \frac{\int f(\nu - \delta)\nu^3 d\nu}{\int f(\nu - \delta)d\nu} \quad (3.47)$$

and the site distribution function is assumed to follow a Gaussian distribution:

$$p(\delta) = (2\pi\sigma^2)^{-\frac{1}{2}} \exp\left[-\frac{(\delta - \delta_0)^2}{2\sigma^2}\right] \quad (3.48)$$

where σ denotes the variance of the distribution and δ_0 the average shift induced by the polar solvent. Now by measuring the absorption and emission spectra in a non-polar solvent, the lineshape functions $g(\nu)$ and $f(\nu)$ can be calculated using equations 3.45 and 3.46. Then $p(\delta)$ is calculated using equations 3.45 and 3.43 and the absorption spectrum A_p taken in the polar solvent of interest. Thus the time-zero spectrum can be calculated using Equation 3.44.

A simplified method to calculate the time-zero spectrum can be used when the excitation occurs in the absorption maximum and the absorption spectrum is not highly structured. In this case, nearly no selection of the different solvation states occurs and thus neither the details of the width of the site distribution nor those of the homogeneous spectrum have to be considered [36]. In this case the time-zero spectra can be obtained using:

$$\nu_p(t = 0) \approx \nu_p(abs) - (\nu_{np}(abs) - \nu_{np}(em)) \quad (3.49)$$

where “*p*” refers to the polar and “*np*” to the non-polar spectrum. To verify the described method, Maroncelli et al. used probes in a glass matrix of frozen solvents. In a glass matrix, the solvent relaxation is very slow or perhaps even completely stopped, and one can obtain the time-zero spectrum directly. In this way it was shown that the uncertainty of the described method lies in the order of approximately 200 cm^{-1} for the emission maxima of the time-zero spectra. The deviations between the time-zero spectra obtained using the simplified method and those obtained using the full approach are in the order of $\pm 50\text{ cm}^{-1}$ for the emission maxima.

3.4 Lipid bilayers

Biological membranes have been studied extensively, being of great interest as the main component of every living cell. Lipid bilayers are the basic structure of many biological membranes. Incorporation of fluorescent probes into such lipid bilayers helped to understand the bilayers structure and properties. The ability of lipids to form self-organised bilayers can be used to orientate the fluorophores.

3.4.1 Lipids

Lipids are organic compounds which are insoluble in water. In “The Lipid Handbook” by Gunstone, Harwood and Padley, several thousand lipids are described [37]. This section will focus on membrane lipids and especially on phospholipids. Membrane lipids are amphiphilic molecules consisting of a hydrophilic head group and a hydrophobic tail. The tail consists of one or two alkyl or alkenyl chains, usually consisting of twelve to twenty-four carbon atoms. Because of their amphiphilic character, lipids form bilayers or micelles in an aqueous environment, so that the hydrophobic tails are shielded from surrounding water. Lipids with one alkyl chain tend to form micelles, while lipids with two alkyl chains tend to form bilayers. These bilayers can occur in different forms, for example, unilamellar and multilamellar vesicles (liposomes). In Figure 3.7, several aggregates formed by lipids with one or two alkyl chains can be seen. When a chain contains one or more *cis*-double bonds, the chain will be twisted. This twisting, as well as the chain length, affect the fluidity of a membrane.

The lipid used in this work is 1,2-dipalmitoyl-*sn*-glycero-3-phosphocholine (DPPC). DPPC has two saturated alkyl chains of sixteen carbon atoms each (Figure 3.8). DPPC appears in many different phases depending on the level of hydration, temperature, pH value, pressure and salt concentration [39–41]. In this project we work with fully hydrated DPPC and its $L_{\beta'}$, $P_{\beta'}$ and L_{α} phases. In the $L_{\beta'}$ or gel-phase, the alkyl chains, which are in an all-*trans* conforma-

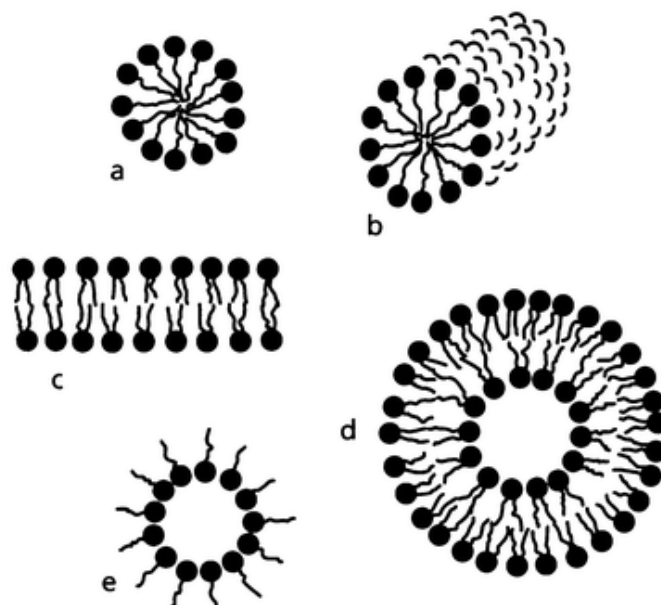


Figure 3.7: Various possible aggregates of lipids: micelle (a), cylindrical micelle (b), bilayer (c), vesicle (d) and inverted micelle (e). From [38].

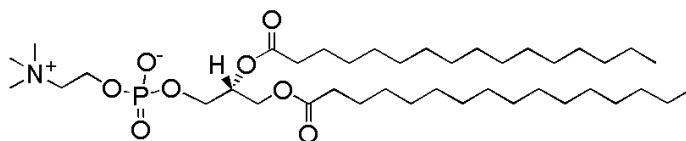


Figure 3.8: 1,2-dipalmitoyl-*sn*-glycero-3-phosphocholine (DPPC).

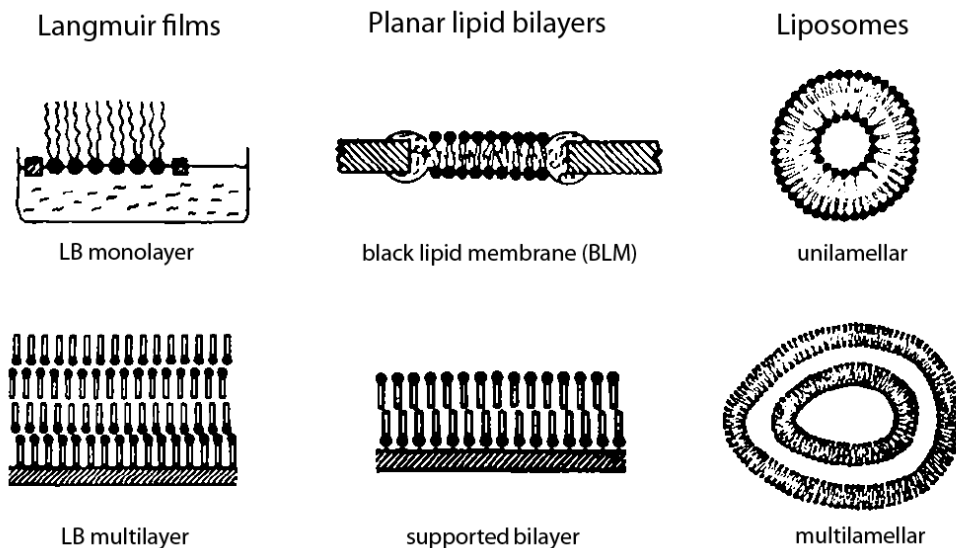


Figure 3.9: Different membrane systems; from [42].

tion, are tilted with respect to the bilayer normal, and the long axis of the head group is oriented parallel to the bilayer plane [39]. Upon heating, the $L_{\beta'}$ phase undergoes a phase transition: the pretransition to the $P_{\beta'}$ or rippled-phase. After further heating, the main transition $P_{\beta'}$ to L_{α} occurs. In the L_{α} or liquid-crystalline phase, the chains are in a gauche conformation and the volume per lipid for DPPC increases from around 1140 \AA^3 to around 1230 \AA^3 [40]. The phase transition temperatures for fully hydrated DPPC at a pH value of 7 and a salt concentration $<0.1 \text{ M}$ are $(34.4 \pm 2.5)^{\circ}\text{C}$ for the $L_{\beta'} \rightarrow P_{\beta'}$ transition and $(41.3 \pm 1.8)^{\circ}\text{C}$ for the $P_{\beta'} \rightarrow L_{\alpha}$ transition [39].

Model systems for the described lipid bilayers include Langmuir-Blodgett films, black lipid membranes (BLM), supported planar monolayers and supported planar bilayers, small unilamellar vesicles (SUV), large unilamellar vesicles (LUV) and multilammellar vesicles (Figure 3.9).

Reference [42] introduces and describes the systems in detail. The membrane systems used in this work are unilamellar vesicles, supported planar bilayers and supported planar monolayers on pre-coated hydrophobic glass slides.

Vesicles

Bangham et al. [43] first reported liposomes in which the lipids are organised in concentric lamella, each separated from its neighbor by a water lamellae. The described liposomes vary in diameter from several hundred angstroms to several microns. Huang [44] introduced another form of liposome dispersion: single spherical bimolecular lamellae which are homogeneous in size. These

lamellae enclose a volume of aqueous solution and are called unilamellar vesicles. Small unilamellar vesicles are usually produced in two steps. First, large multilamellar vesicles (LMV) are produced by the method described by Bangham [43]. In the second step, a modified version [45] of the method introduced earlier by Huang et al. [46] is applied. Basically, the LMVs are sonicated to obtain unilamellar vesicles and then centrifuged to obtain SUVs. To characterise the size of the resulting vesicles, dynamic light scattering (DLS) can be used. A particle in a suspension undergoes Brownian motion induced by collisions with solvent molecules. The larger a particle is, the more slowly it moves in reaction to these collisions. When the probe is illuminated, the intensity of the scattered light fluctuates differently for particles of different sizes, and thus, velocities. Thus, by measuring the scattered light, it is possible to calculate the radius of the light-scattering particles.

Supported planar layers

The formation of supported planar lipid layers uses hydrophobic or hydrophilic driving forces. On a hydrophobic surface, for example glass slides coated with alkanethiol monolayers [47] which are in contact with a vesicle suspension, the vesicles fuse to the hydrophobic part. A lipid monolayer is generated in which the hydrophobic chains point toward the surface and the hydrophilic head regions point toward the aqueous solution. The same self-assembly principle occurs on a hydrophilic surface (for example a blank glass slide), except that here a bilayer is generated, with a first layer in which the hydrophilic head regions point toward the surface followed by another layer with the head regions pointing toward the aqueous solution. In both cases a hydrophilic surface is generated. The principles and requirements of the surfaces and vesicles have been studied extensively [47–56]. Methods of characterising surfaces include atomic force spectroscopy, ellipsometry and contact angle measurements.

Many methods for characterising lipid bilayers are based on fluorescence probes which are incorporated in or in contact with the bilayer. In this work the interactions between a phospholipid bilayer and a particular set of fluorophores will be studied.

3.4.2 Fluorescence probes in lipid bilayers

Fluorescence probes with readily interpretable emission properties can be specifically inserted into biological macromolecules. The emission characteristics of many fluorophores are responsive to their microenvironment. In this way they can be used to probe the polarity, viscosity, rotational mobility and geometry of biological membranes. Waggoner and Stryer [57] first used 12-(9-Anthroyl)-stearic acid (see Figure 3.10) to probe particular regions of vesicles composed of phosphatidylcholine. To allow the investigation of different re-

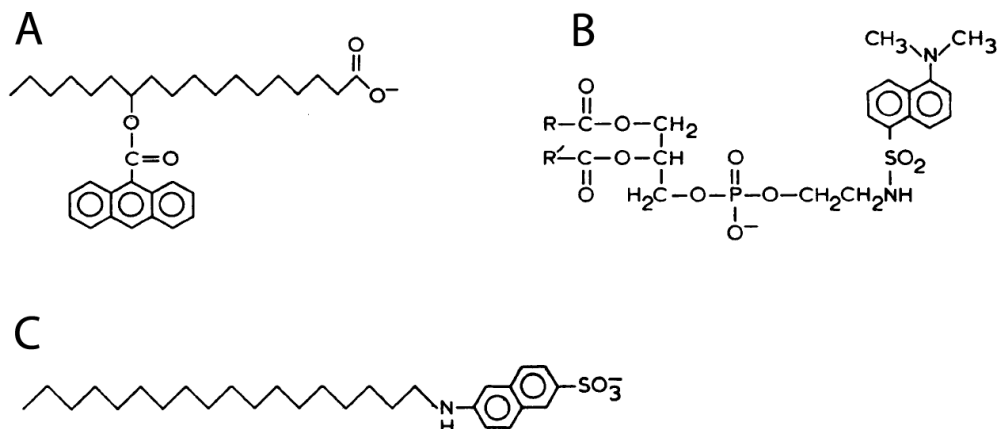


Figure 3.10: Fluorescent probes designed by Waggoner et al. [57]. A, anthroyl stearic acid; B, dansyl phosphatidyl ethanolamine; C, octadecyl naphthylamine sulfonate. *R* and *R'* in B are long-chain fatty acid residues.

gions of the bilayers, the fluorescence probes must fulfill the following criteria [57]: first, they need to have a high affinity for bilayer regions. Therefore each probe has a long alkyl chain to interact with the phospholipid molecules in the bilayer. Second, the probes must have distinct polar and non-polar regions to orient them with respect to the bilayer normal. In the probes A and C (Figure 3.10), the ionic head group acts as the polar part, while in B a phosphatidyl headgroup (similar to that of the lipids) is used. Third, the emission spectra of the probes must be sensitive to the polarity of its environment. Waggoner et al. measured the emission spectra of these probes in solvents of different polarity and incorporated in bilayers. Comparing these spectra allowed them to draw conclusions about the position of the probes within the bilayer. Thulborne and Sawyer [18] examined a set of four (n-(9-anthroyloxy) fatty acids (Figure 3.11) with $n = 2, 6, 9, 12$, using polarisation measurements to obtain their rotational relaxation times. Quenchers were used to gain information about the position of the probes within the bilayer. A quenched probe is by definition accessible by a quencher. Quenchers which cannot penetrate a lipid bilayer can only quench probes close to its surface, whereas the quenching efficiency of hydrophobic quenchers is highest for probes in the center of the bilayer. Using a modified Stern-Volmer plot and hydrophobic and hydrophilic quenchers, Thulborne and Sawyer [18] could draw conclusions about the position of the fluorophores within the bilayer. Using this information, they could show that the change in microviscosity after phase transition from the gel phase to the liquid crystalline phase is higher toward the center of the bilayer.

Easter, DeToma and Brand [58–60] developed and described a method to characterise the time evolution of the red shift occurring after photoexcitation of 2-p-toluidinonaphthalene-6-sulfonate in vesicles of egg lecithin. They in-

Table 3.1: Solvent relaxation times of n-(9-anthroyloxy) fatty acids (Figure 3.11) in DPPC - SUVs in the gel-phase obtained using Equation 3.39 and corresponding Stokes-shifts. From [65].

n	2	6	9	12	16
$\langle \tau_r \rangle / ns$	2.7	3.0	3.6	4.8	5.9
$\Delta (\lambda^{-1}) / cm^{-1}$	1908	1314	971	635	287

terpreted the time-dependent red shift as a result of a “general relaxation of polar residues about the excited chromophore on the nanosecond time scale” [58]. Studies with fluorescence probes in bilayers were able to demonstrate polarity and viscosity gradients in the bilayer. In comparison with bulk-solvents, properties of different regions of the bilayer were characterised. Stationary anisotropy measurements [61] show that the microviscosity of a lipid bilayer decreases toward the center of the bilayer.

Spectral reconstruction, combined with the time-zero estimation (Section 3.3), is a powerful tool to observe the microviscosity and micropolarity of a probe’s environment. Quantitative information about the solvent relaxation time can be obtained for different compositions, parts and states of lipid bilayers. For this purpose, probes have been designed to reach specific regions of the bilayer. In general, it can be said that solvent relaxation time increases toward the center of the bilayer and also with decreasing temperature. Large changes in solvent relaxation time occur during phase transitions of lipid bilayers. Vesicles with a strong curvature (SUVs) show shorter solvent relaxation times than LUVs.

These effects can be understood by considering the water gradient in the bilayer normal [28]. A polarity gradient in the vicinity of a bilayer is due to the presence of water molecules hydrating the membrane. Even in the center of the bilayer, water molecules have been detected [62], in contradiction to theoretical simulations [63]. Hof et al. [28] assume that the high dipole moment of the excited molecule in the center of the bilayer draws water molecules toward itself from outer regions of the bilayer. A decreased microviscosity toward the center [61] appears to contradict increasing solvent relaxation times. If the solvent relaxation mechanism is understood as a result of diffusing water molecules, then an increasing solvent relaxation time reflects decreasing mobility of water molecules toward the bilayer center. Strong curvature of the membrane results in a higher mobility of water molecules and thus in decreased solvent relaxation times. Table 3.1 lists relaxation times and Stokes-shifts of a set of n-(9-anthoyloxy) fatty acids in DPPC-vesicles. The solvent relaxation time increases toward the center of the bilayer due to decreased mobility of water molecules. The Stokes-shift decreases due to decreased mi-

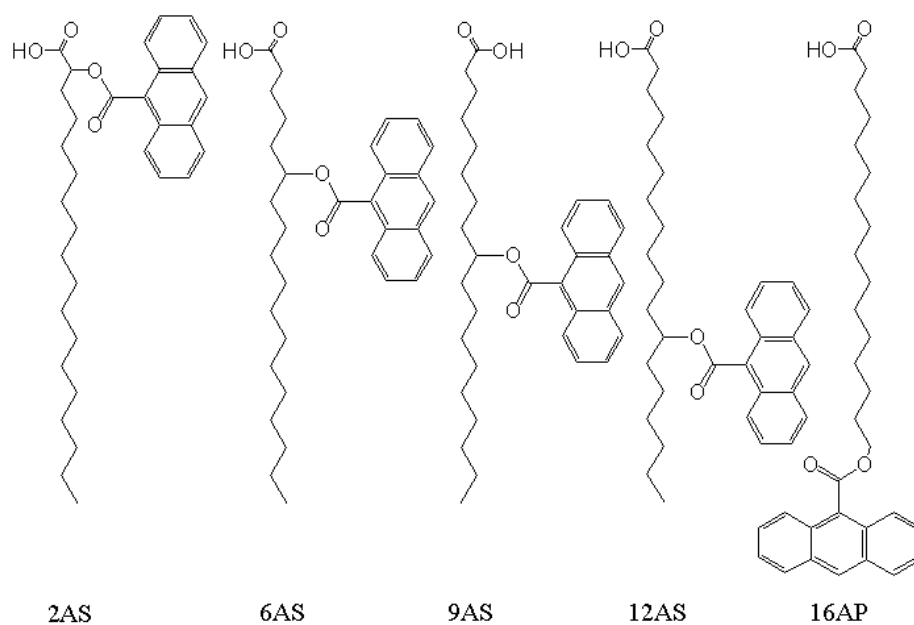


Figure 3.11: From the left: 2-(9-anthroyloxy)stearic acid (2AS), 6-(9-anthroyloxy)stearic acid (6AS), 9-(9-anthroyloxy)stearic acid (9AS), 12-(9-anthroyloxy)stearic acid (12AS), 16-(9-anthroyloxy)palmitic acid (16AP). After [64].

cropolarity toward the lipid bilayer center.

Chapter 4

Results and discussion

4.1 Pyrene-acceptor probes in homogeneous solvent environments

The molecules used in this work are closely related to 2,5E-PP, which was shown to form an excited charge transfer state [13]. For this work, to achieve a preferential orientation of a charge transfer system in lipid bilayers, a set of three different probes was synthesised based on the same donor-acceptor system as in 2,5E-PP. To characterise the effects of their structural differences of the probes on the photophysics and especially the excited charge transfer, UV/Vis absorption and steady-state and time-resolved fluorescence measurements in solvents of different polarity and in protic solvents were undertaken and will be described in this section.

The structure of the probes used in this work can be seen in Figure 4.1 and Figure 4.2. They are based on the chromophore 1-phenylpyrene (PhP, Figure 4.3). The probes are modified to allow an incorporation into a lipid bilayer. The ionic head group serves as the hydrophilic part and the length of the alkyl chain causes a specific positioning of the probes in the lipid bilayer and contributes to the hydrophobic part.

A preliminary characterisation of the structure and conformation of the probes can be achieved using AM1 semiempirical calculations. The results are given in Table 4.1. The dihedral angles between the phenyl and the pyrene moiety are larger than in PhP due to sterical influences of the ester groups. The ester groups also slightly increase the ground state dipole moment of PA3, PA5 and PA11 compared to PhP.

4.1.1 UV/Vis absorption and fluorescence spectra

Figure 4.4 shows the absorption and fluorescence spectra of pyrene, PhP and PA5 in THF. Both pyrene and PhP show structured absorption and fluores-

Table 4.1: Calculated probe parameters. μ_g is the ground state dipole moment, r is the longest molecule axis. α describes the dihedral angle between the pyrene and the phenyl ring. r , μ_g and α were calculated using Ampac [66] AM1 semiempirical calculations. a denotes the Onsager radius, estimated as half the distance between the C(1) atom of the pyrene moiety and the carbon atom of the ortho-ester group after semiempirical AM1 calculations. μ^* and μ_ρ^* are the excited state dipole moments, calculated with Equation 3.35, the slope of $\nu_f/\Delta f'$, where ν_f is the emission maximum and $\Delta f'$ the polarity function calculated using Equation 3.36 and the Onsager radius a after estimation and a_ρ calculated using Equation 3.37.

Compound	α	μ_g /D	r /Å	ρ^a /g cm ⁻³	a_ρ /Å	a /Å	$\nu_f/\Delta f'^b$ /cm ⁻¹	μ^* /D	μ_ρ^* /D
PhP ^c	56.9	0.14	10		5.5	5.5	-300	2.1	
PA0	61.2	1.3	12	1.30	6.1	6.1			
PA3	61.2	3.47	14.6	1.27	6.4	6.1	-23700	21.0	22.4
PA5	61.4	3.52	17.4	1.23	6.6	6.1	-23900	21.1	23.5
PA11	61.2	3.29	24.6	1.15	7.1	6.1	-23700	20.9	25.8

^acalculated with ACD [67]

^berror less than 10%

^cdata taken from [13]

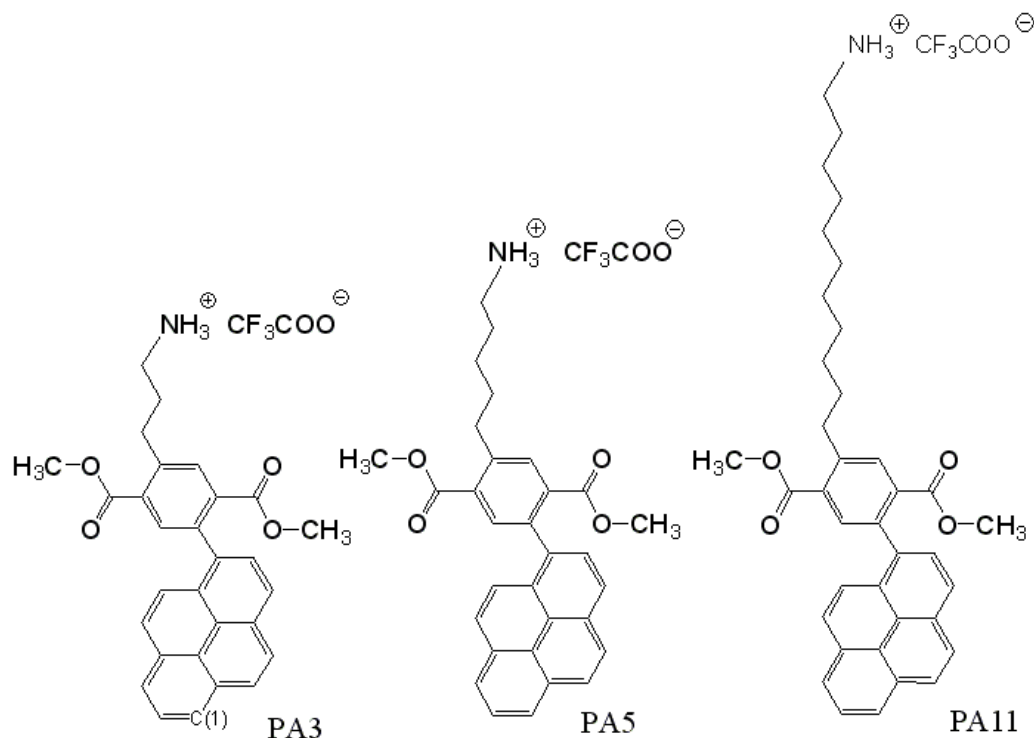


Figure 4.1: Chemical structures of the ammonium salts of dimethyl 2-(3-aminopropyl)-5-(pyren-6-yl)benzene-1,4-dioate (PA3), dimethyl 2-(5-aminopentyl)-5-(pyren-6-yl)benzene-1,4-dioate (PA5), dimethyl 2-(11-aminoundecyl)-5-(pyren-6-yl)benzene-1,4-dioate (PA11). The position of the C(1) atom of the pyrene moiety is marked in the structure of PA3.

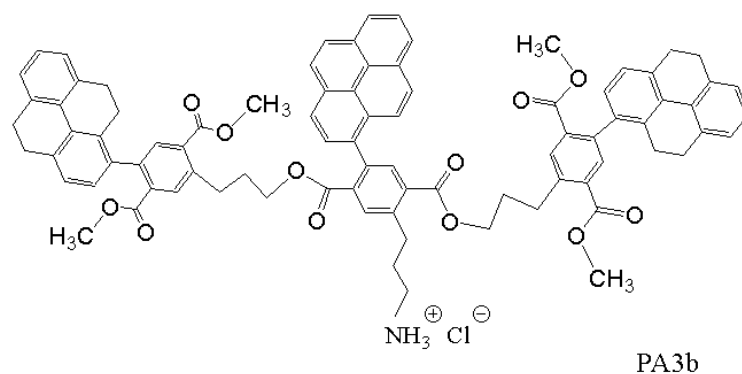


Figure 4.2: Chemical structure of the ammonium salt of 1,4-benzenedicarboxylic acid, 2-(3-aminopropyl)-5-(1-pyrenyl)-, bis[3-[2,5-bis(methoxycarbonyl)-4-(4,5,9,10-tetrahydro-1-pyrenyl)phenyl]propyl]ester (PA3b).

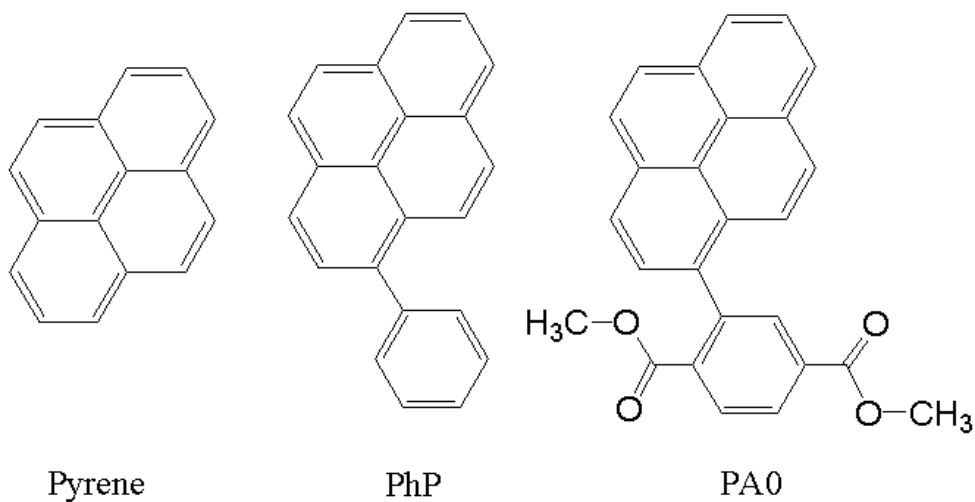


Figure 4.3: From left: structure of the parent chromophores pyrene, 1-phenylpyrene (PhP) and dimethyl 2-(pyren-1-yl)benzene-1,4-dioate (PA0).

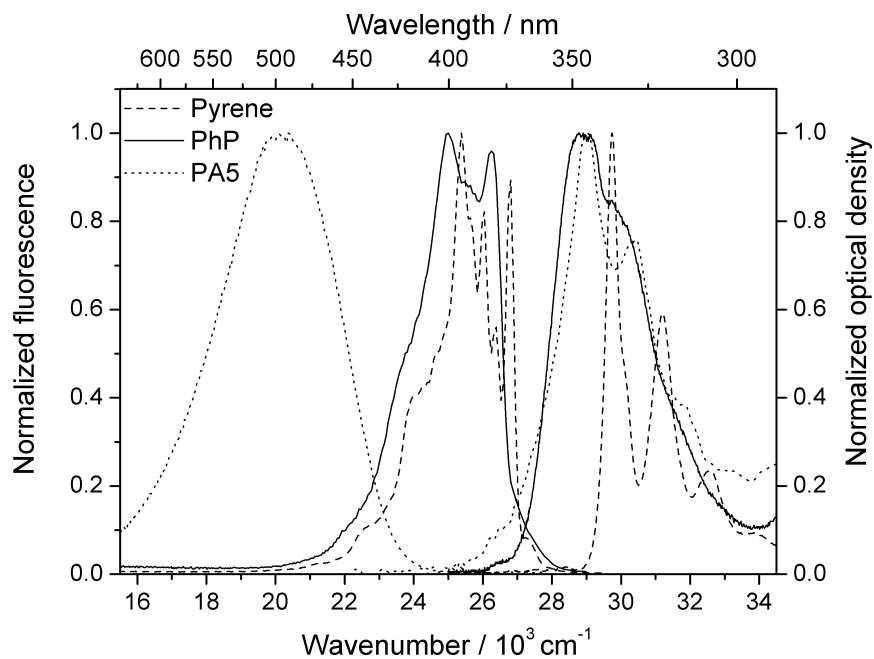


Figure 4.4: Comparison of the UV/Vis absorption and fluorescence spectra of pyrene, PhP and PA5 in THF.

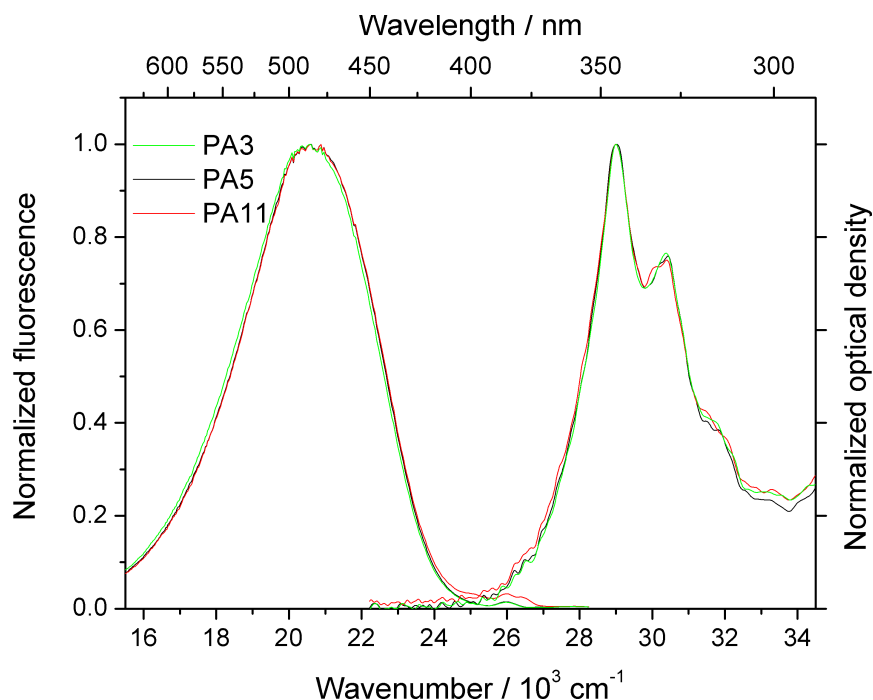


Figure 4.5: Normalised UV/Vis absorption and fluorescence spectra of PA3, PA5 and PA11 in THF.

cence spectra approximately following the mirror image rule. The absorption spectrum of PA5 is slightly red shifted to the pyrene absorption spectrum but has a high conformity with the PhP absorption spectrum, indicating that for PA5, the PhP moiety is the absorbing chromophore of the molecule. The fluorescence spectrum of PA5 is structureless and shows a strong red shift compared to the fluorescence spectrum of PhP, indicating that it forms an excited state different from that of PhP.

While the absorption- and fluorescence spectra of PhP and PA5 differ in the same solvent, no significant differences in the absorption spectra of PA3, PA5 and PA11 in the same solvent were found. Figure 4.5 shows the absorption and fluorescence spectra of PA3, PA5 and PA11 in THF. The emission maxima of PA3, PA5 and PA11 in the same solvent differ slightly in position (Table 4.2).

In Figure 4.6 one can see that the absorption spectra of PA5 have the same structure and peak position in DE, THF, EtOH and ACN. This is also the case for PA3 and PA11. Despite their ionic head group the compounds are not soluble in water. In n-hexane, the solubility of PA3, PA5, PA11 and PA3b was too poor for resolution of the UV/Vis absorption spectra, while the fluorescence excitation spectra indicated absorption maxima similar to those measured in other solvents. This lack of a solvatochromic shift in the absorption spectra indicates that there is only a small difference between the dipole moments in the ground state and the excited Franck-Condon state of the four probes.

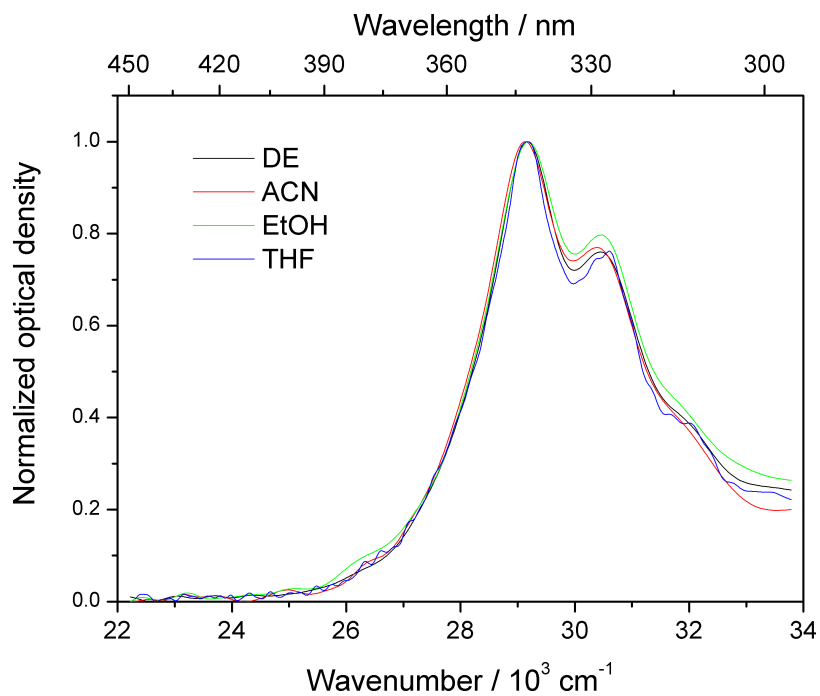


Figure 4.6: Normalised UV/Vis absorption spectra of PA5 in solvents of different polarity.

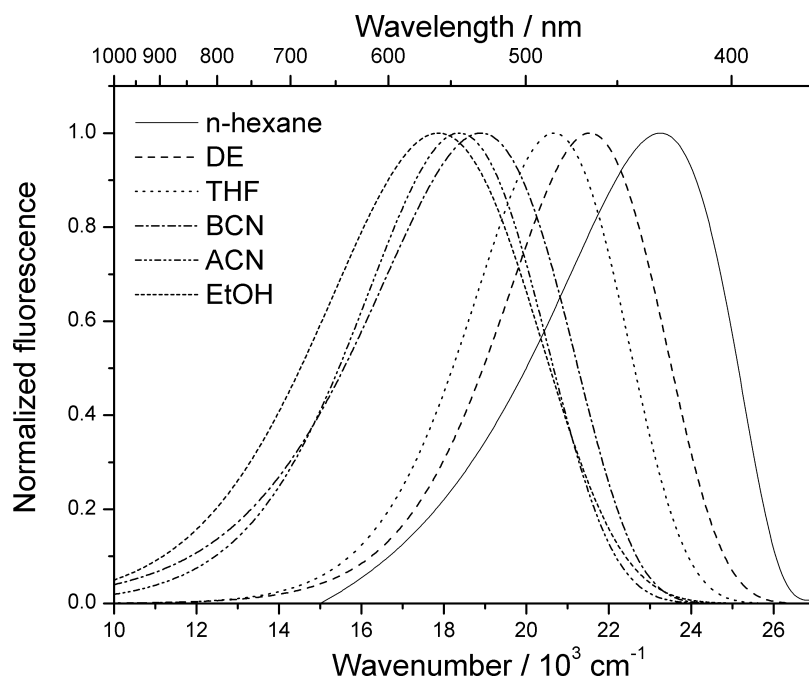


Figure 4.7: Fluorescence spectra of PA5 in solvents of different polarity.

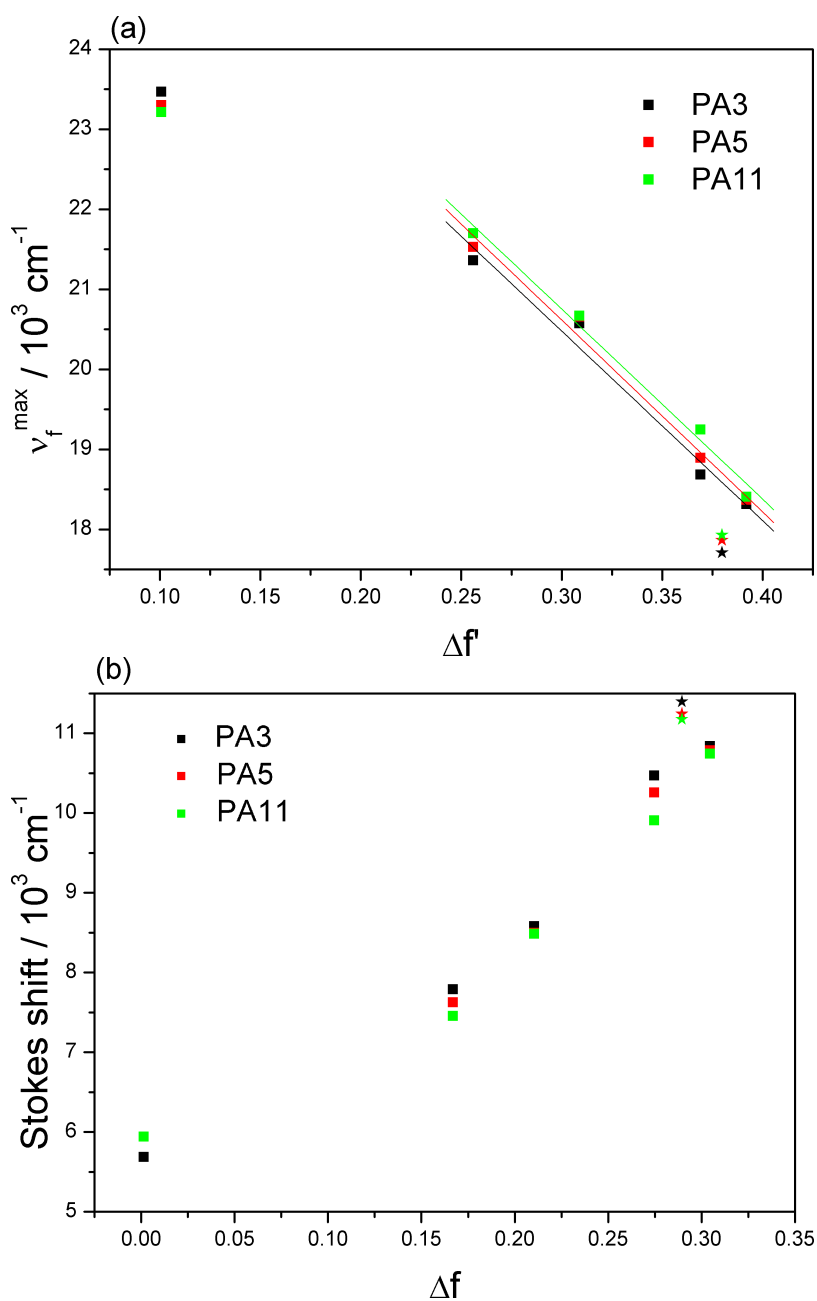


Figure 4.8: Emission maxima (a) and Stokes shifts (b) as a function of the solvent polarity function $\Delta f'$ and Δf , respectively. The solvents were *n*-hexane, DE, THF, BCN and ACN (from left to right). The slopes in (a) were calculated, using a linear fit, as -23670 cm^{-1} , -23954 cm^{-1} and -23730 cm^{-1} for PA3, PA5 and PA11, respectively. Stars represent the the values in EtOH.

Although solvent polarity does not affect the absorption spectra, we see a strong effect of solvent polarity on the fluorescence spectra. In Figure 4.7 the fluorescence spectra of PA5 in solvents of different polarity can be seen. Figure 4.8 shows the emission maxima and the Stokes shifts of PA3, PA5 and PA11 as a function of the solvent polarity Δf . The shifts of the emission maxima over $\Delta f'$ allow the calculation of the excited state dipole moment (Equations 3.35 and 3.36). The results are given in Table 4.1. The calculated excited state dipole moment is highly dependent on the Onsager radius a . Using Equation 3.37, a was calculated as 6.4 Å, 6.6 Å and 7.1 Å for PA3, PA5 and PA11, respectively. These differences in a should lead to different excited state dipole moments, dependent on the length of the alkyl chain. However, the slopes in Figure 4.8 are very similar and indicate that the excited state dipole moments do not differ between the three probes. Another estimation of a is half the distance of the atoms of the molecule which provide the strongest dipole vector component [25, 26]. We assume that the alkyl chain does not contribute to the dipole moment and thus the distance between the C(1) atom of the pyrene moiety to the oxygen atom of the ester group was used: $a = 6.1$ Å. This approach for the estimation of a is consistent with the Onsager radius used for D-A biphenyls reported in [14, 68–70] and with the Onsager radius of PA0 calculated using Equation 3.37. In [13] an Onsager radius of $a = 6.9$ Å was determined for 2,5E-PP (Figure 3.1) using Equation 3.37. The high excited state dipole moments for PA3, PA5 and PA11 of around 21 D (Table 4.1) indicate that an excited charge transfer state exists.

4.1.2 Fluorescence quantum yields and decay times

The measurement of the fluorescence decay time τ and the quantum yield Φ_f allows the calculation of the radiative and non-radiative rate constants k_{nr} and k_f (Equations 3.3 and 3.4), and thus the fluorescence transition dipole moment M_f (Equation 3.7). The fluorescence decay times were obtained using the method of TC-SPC. The quantum yields were obtained by measuring against quinine bisulfate as a quantum yield standard. The results of the measurements of τ and Φ_f are given in Table 4.2.

In Figure 4.9, the k_f values of the four probes are shown in solvents of different polarities. Notable is the decrease of k_f with increasing polarity and the value of k_f in ethanol which do not fit the pattern. This decrease implies a decrease of M_f , which can be explained by a pre-twisting of the already twisted compounds and thus a weakening of the conjugation between the pyrene moiety and the phenyl-ester moiety. In Figure 4.10 the k_{nr} values are shown to be only weakly dependent on the solvent polarity. Again, the values for k_{nr} in ethanol seem not to follow the tendency of the other solvents.

The unusual results in ethanol are important, considering that ethanol is a protic solvent and thus able to form H-bonds. Because the probes will later

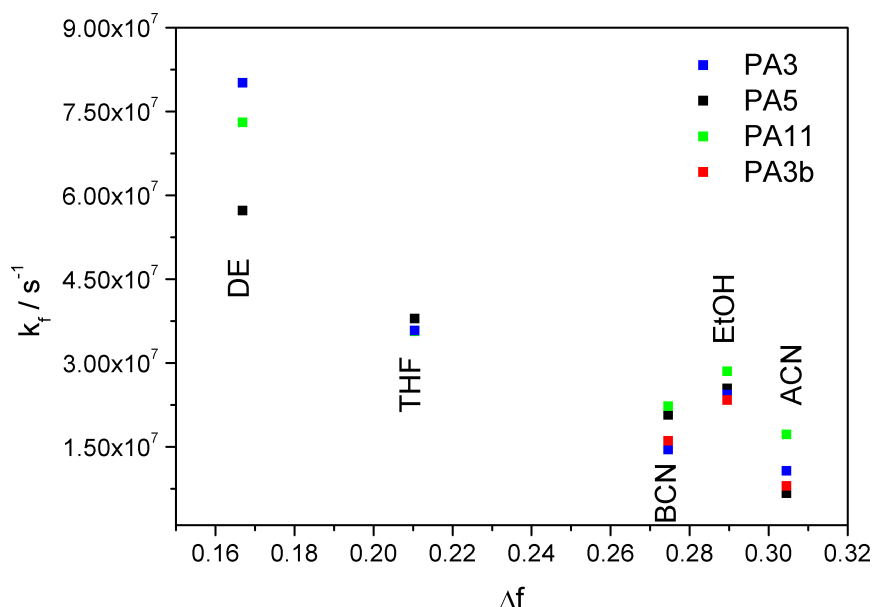


Figure 4.9: Radiative rate constants of PA3, PA5, PA11 and PA3b in solvents of different polarity and in the protic solvent EtOH.

be incorporated into vesicles and thus be in an aqueous environment in which H-bonding can also occur, the influences of H-bonding effects therefore should first be examined. Figure 4.11 and 4.12 show a comparison of the rate constants of the probes in non-protic solvents and in water-ACN mixtures of different ratios. It can be seen clearly that the non-radiative rate constant k_{nr} increases strongly as water concentration increases, whereas the radiative rate constant k_f shows no noticeable dependence. Figure 4.12 shows that the non-radiative rate constant increases less for the probe PA3b. The Δ_f value for the water-ACN mixture is calculated as:

$$\Delta f(ACN + H_2O) = \frac{\Delta f(H_2O)[H_2O] + \Delta f(ACN)[ACN]}{[H_2O] + [ACN]} \quad (4.1)$$

The difference in Δ_f values in plain ACN ($\Delta_f = 0.305$) to a 1:1 water-ACN mixture ($\Delta_f = 0.312$) is slight.

The physical parameters obtained also show that the alkyl chain has only a very small effect on the excited state relaxation behaviour of the probes. The fluorophores are highly sensitive to solvent polarity and form a charge transfer excited state.

4.1.3 Quenching effects of protic solvents

In the last section it was shown that protic solvents have strong influences on the photophysics of the probes. In this section we therefore examine the effects

Table 4.2: Absorption and fluorescence maxima of PA3, PA3b, PA5 and PA11 in different solvents. Fluorescence decays were measured at emission maxima and the values of τ were calculated from monoexponential fits of TC-SPC data. Φ_f is the fluorescence quantum yield and k_{nr} and k_f are the nonradiative and radiative rate constants, respectively. M_f denotes the fluorescence transition dipole moment.

Solvent	Probe	ν_{abs}^a / $10^3 cm^{-1}$	ν_f^b / $10^3 cm^{-1}$	τ^c /ns	Φ_f^d	k_{nr} / $10^8 s^{-1}$	k_f / $10^7 s^{-1}$	M_f^e /D
n-hexane	PA3	(29.16) ^f	23.48	0.9				
	PA5	(29.16)	23.30	1				
	PA11	(29.16)	23.21	1.1				
DE	PA3	29.16	21.36	3.5	0.28	2.05	8.0	1.02
	PA5	29.16	21.54	3.3	0.19	2.5	5.7	0.86
	PA11	29.16	21.70	3.0	0.22	2.64	7.31	0.96
	PA3b	29.16	21.47					
THF	PA3	29.16	20.51	5.5	0.20	1.47	3.6	0.70
	PA5	29.16	20.57	5.4	0.21	1.46	3.8	0.71
	PA11	29.16	20.67	5.8	0.21	1.36	3.56	0.68
	PA3b	29.16	20.90					
BCN	PA3	29.16	18.69	2.1	0.03	4.6	1.45	0.52
	PA5	29.16	18.90	2.5	0.05	3.77	2.07	0.61
	PA11	29.16	19.25	2.8	0.06	3.4	2.2	0.61
	PA3b	29.16		2.4	0.04	4	1.6	
ACN	PA3	29.16	18.32	2.4	0.02	4.1	1.0	0.46
	PA5	29.16	18.40	1.8	0.01	5.6	0.67	0.38
	PA11	29.16	18.41	2.0	0.04	4.75	1.7	0.60
	PA3b	29.16	19.13	2.6	0.01	3.7	0.8	
EtOH	PA3	29.16	17.71	0.7	0.02	14	2.4	
	PA5	29.16	17.87	0.7	0.02	13	2.5	
	PA11	29.16	17.93	0.8	0.02	12	2.8	
	PA3b	29.16	18.73	1.3	0.03	7.8	2.3	

^aerror appr. $0.02 \cdot 10^3 cm^{-1}$

^berror appr. $0.04 \cdot 10^3 cm^{-1}$

^cerror appr. ± 0.1 ns

^derror appr. $\pm 15\%$

^eafter Equation 3.7

^fvalues in parentheses are estimated from excitation spectra because of poor solubility of probes in n-hexane

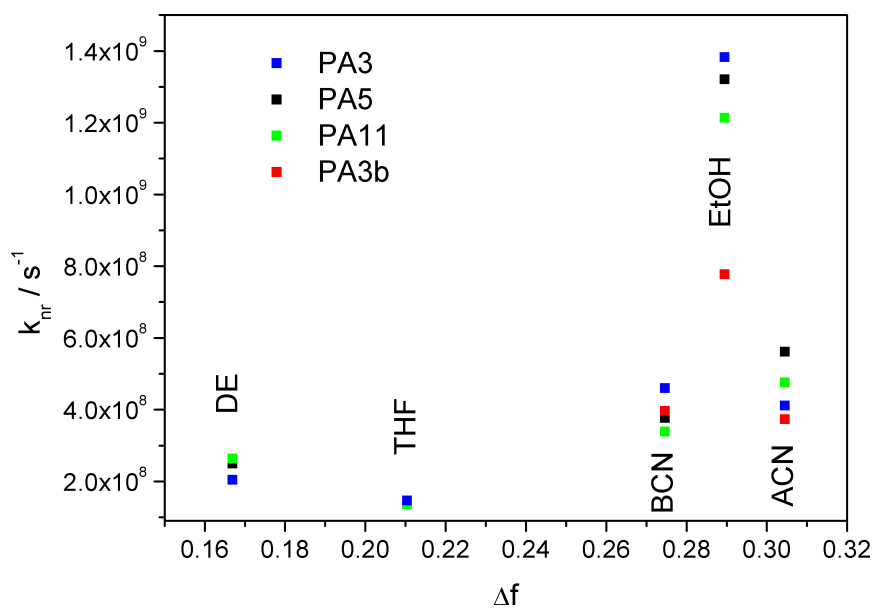


Figure 4.10: Nonradiative rate constants of PA3, PA5, PA11 and PA3b in solvents of different polarity and in the protic solvent EtOH.

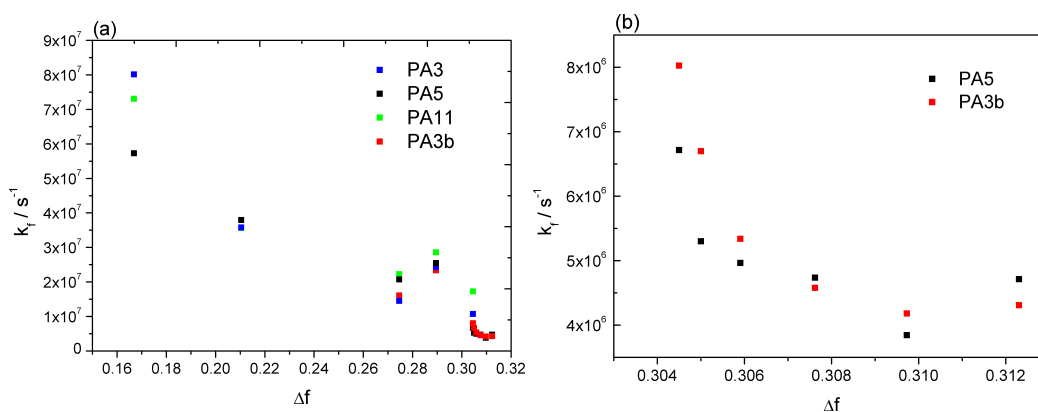


Figure 4.11: Radiative rate constants of PA5 and PA3b in a water-ACN mixture of different ratios in comparison with the radiative rate constants of PA3, PA5, PA11 and PA3b in non-protic solvents (a). Nonradiative rate constants of PA5 and PA3b in a water-ACN mixture of different ratios (b). The Δf value for the water-ACN mixture is calculated as the weighted mean value.

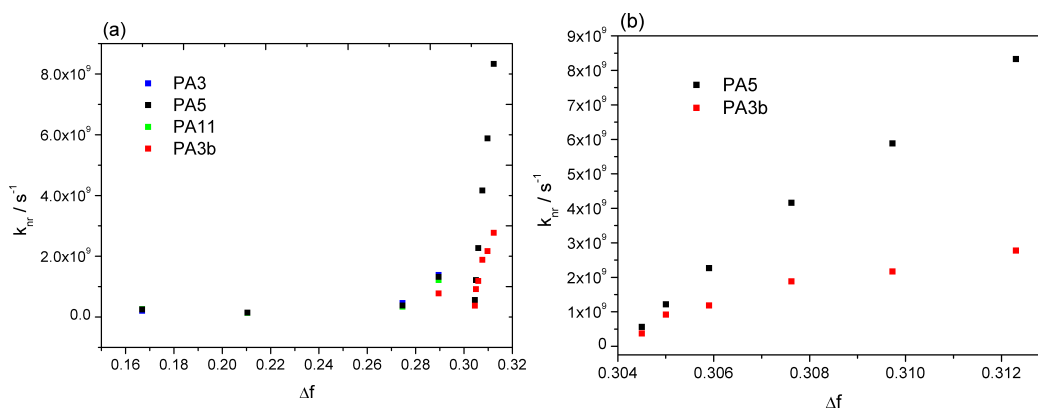


Figure 4.12: Nonradiative rate constants of PA5 and PA3b in a water-ACN mixture of different ratios in comparison with the radiative rate constants of PA3, PA5, PA11 and PA3b in non-protic solvents (a). Nonradiative rate constants of PA5 and PA3b in a water-ACN mixture of different ratios (b). The Δf value for the water-ACN mixture is calculated as the weighted mean value.

of protic solvents on the probes. H-bonding effects between a fluorophore and a solvent can depopulate the electronically excited state of the fluorophore. Assuming that, in our case, water acts as a quencher, we can apply a Stern-Volmer plot to obtain quantitative measurements of the quenching efficiency. In [9] similar quenching effects of protic solvents on highly polar twisting charge transfer states of photoexcited probes were reported. In Figures 4.13 and 4.14, the Stern-Volmer plots of PA5 and PA3b in a water-ACN mixture of different ratios are shown. The rise in τ/τ_0 implies dynamic quenching in both cases (Section 3.1.2). This indicates that the excited state is quenched by the formation of H-bonds.

The downward slope of F_0/F cannot be explained considering only dynamic quenching. In Figures 4.15 and 4.16, modified Stern-Volmer plots are shown, based on the assumption that fractions of the fluorophores are not accessible to the quencher (Section 3.1.2). Using Equation 3.18, the value of the Stern-Volmer quenching constant K is calculated as 1 for PA5 and 0.75 for PA3b. The difference can be understood considering the structure of the probes. The two arms of PA3b seem to hinder the formation of H-bonds between water and the donor acceptor pair of PA3b.

The possibility that a constant fraction of the fluorophore is inaccessible to water molecules is not likely, but the effect of preferential solvation might be capable of explaining the observed downward slope of F_0/F over $[H_2O]$. When two solvents are miscible, it is usually assumed that they form a homogeneous mixture and that solutes are solved by this homogeneous solvent mixture. However, in studies of the solvation of fluorophores in a water-ACN mixture [71, 72], it was reported that fluorophores in low water concentrations are surrounded by an ACN shell; they do not interact with the water molecules.

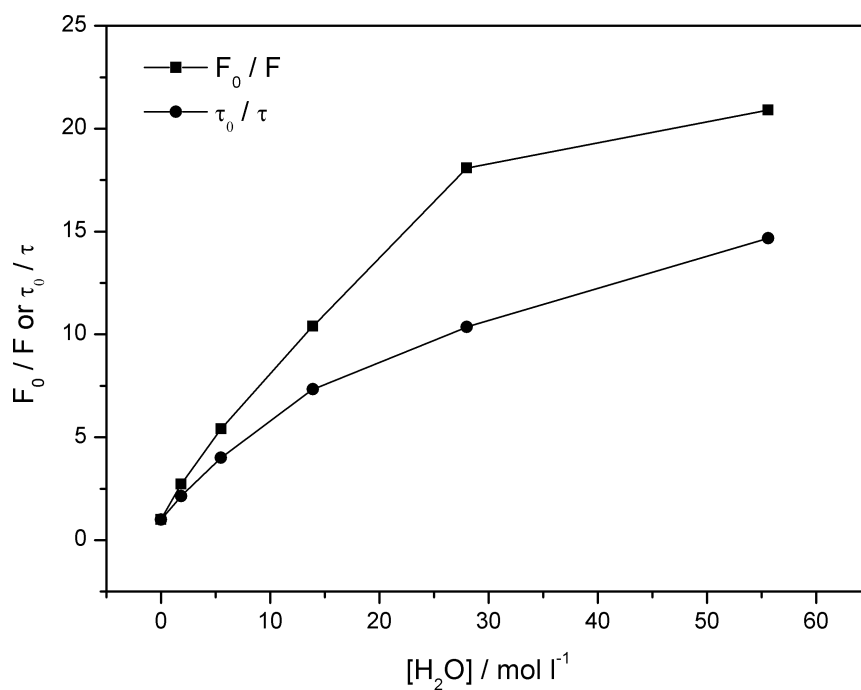


Figure 4.13: Stern-Volmer Plot of PA5 in a water-ACN mixture using Equation 3.8.

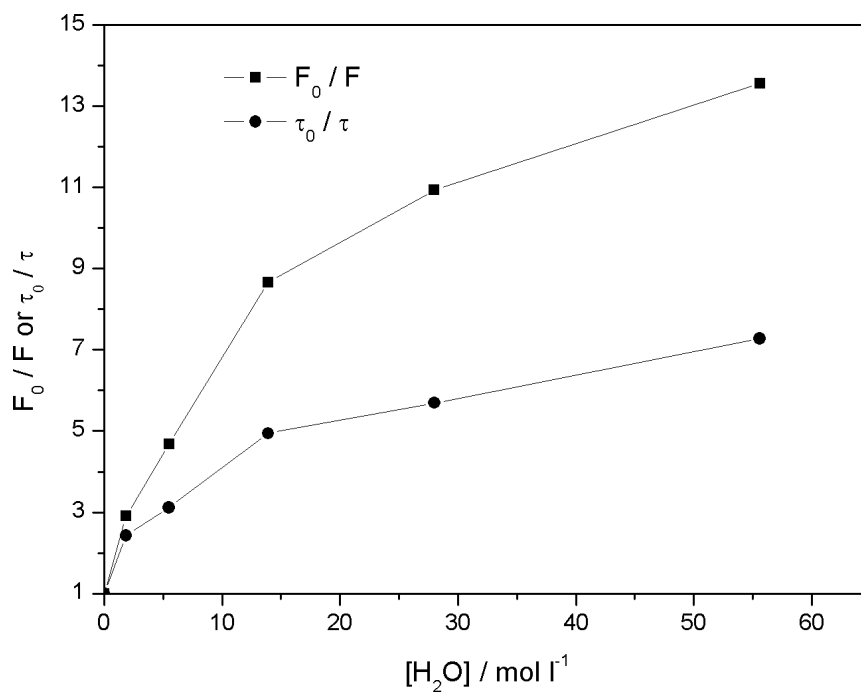


Figure 4.14: Stern-Volmer Plot of PA3b in a water-ACN mixture using Equation 3.8.

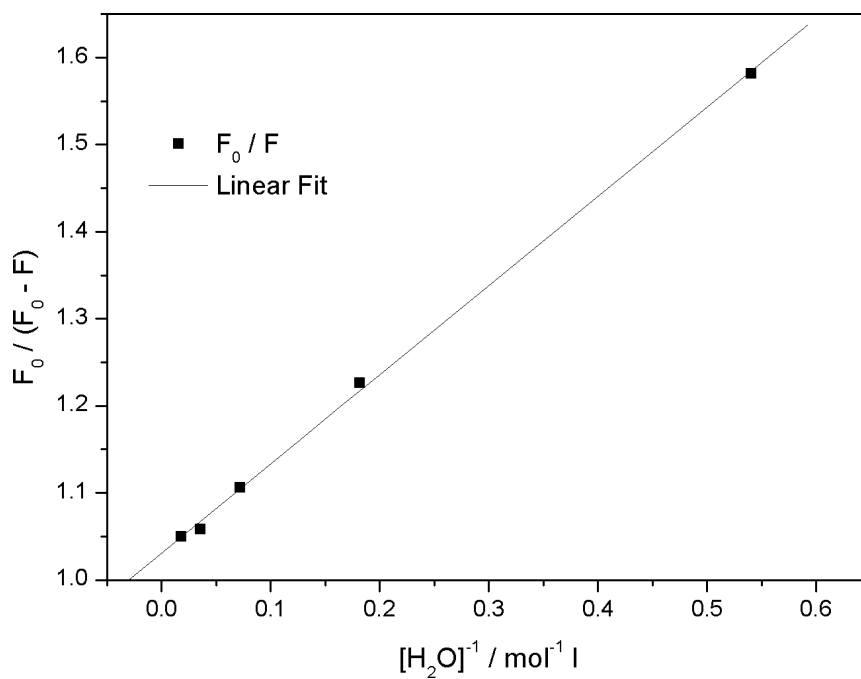


Figure 4.15: Modified Stern-Volmer plot of PA5 in a water-ACN mixture using Equation 3.18.

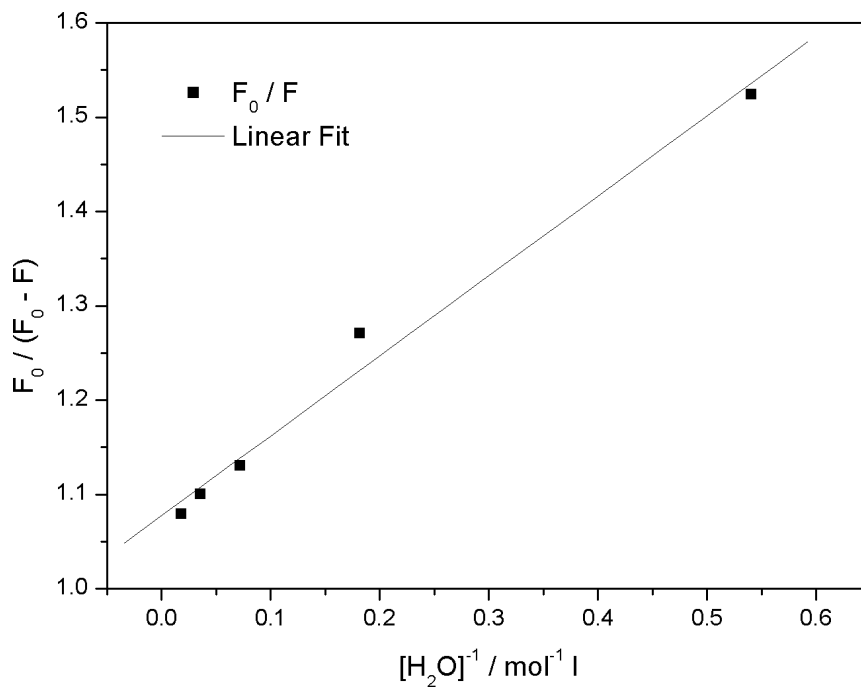


Figure 4.16: Modified Stern-Volmer plot of PA3b in a water-ACN mixture using Equation 3.18.

As the water concentration of the solvent increases, more fluorophores can be influenced by water. At a certain concentration, the effect reverses: the fluorophores are solvated preferentially by water at $[H_2O]/[ACN]>0.85$ [72]. This would mean that in our case fractions of fluorophores are inaccessible to water molecules. At high water concentrations, an upward slope of F_0/F over $[H_2O]$ would be expected because now the molecules are preferentially solved by water. It was not possible to measure this effect because of very low fluorescence gain, but it is clear that water and the formation of H-bonds strongly affect the examined fluorophores fluorescence.

4.2 Pyrene-acceptor probes in phospholipid bilayers

The criteria for fluorescent molecules useful for probing the interior of lipid bilayers are given in Section 3.4.2, and PA3, PA5, PA11 and PA3b fit these criteria. They are highly sensitive to the polarity of their surroundings. They have an ionic headgroup and a hydrophobic alkyl chain. Unlike the anthroyl stearic acids, which have alkyl chains of constant length and a photosensitive part is covalently attached at different positions of the chain, the photosensitive parts of our set of probes are attached to the end of alkyl chains of varying lengths. According to [28, 57], the probes should have the position and orientation shown in Figure 4.17.

4.2.1 Vesicle preparation and characterisation

As a first approach to studying the behaviour of the probes in a lipid bilayer, we used vesicles. Vesicles are easy to make from DPPC and can approximately be treated as planar lipid bilayers, although for very small vesicles, effects from the stronger curvature of the outer vesicle layer need to be considered. In [28] a slight decrease in the solvent relaxation time in SUV's of a diameter of 20 nm was reported. Vesicles in this work were obtained following the method described in Section 3.4.1. Dynamic light scattering experiments were used to measure the size of the vesicles. The vesicles' mean size in different vesicle solutions, after a storage time of appr. 24 h at room temperature, was found to vary between 90 nm and 230 nm. Typical SUV sizes are from appr. 15 nm to 100 nm, LUV sizes are appr. 100 nm to several μm . The differences in the vesicles' mean size are a result of the sonication procedure. The mean vesicle size was not found to be affected by the different incorporated probes.

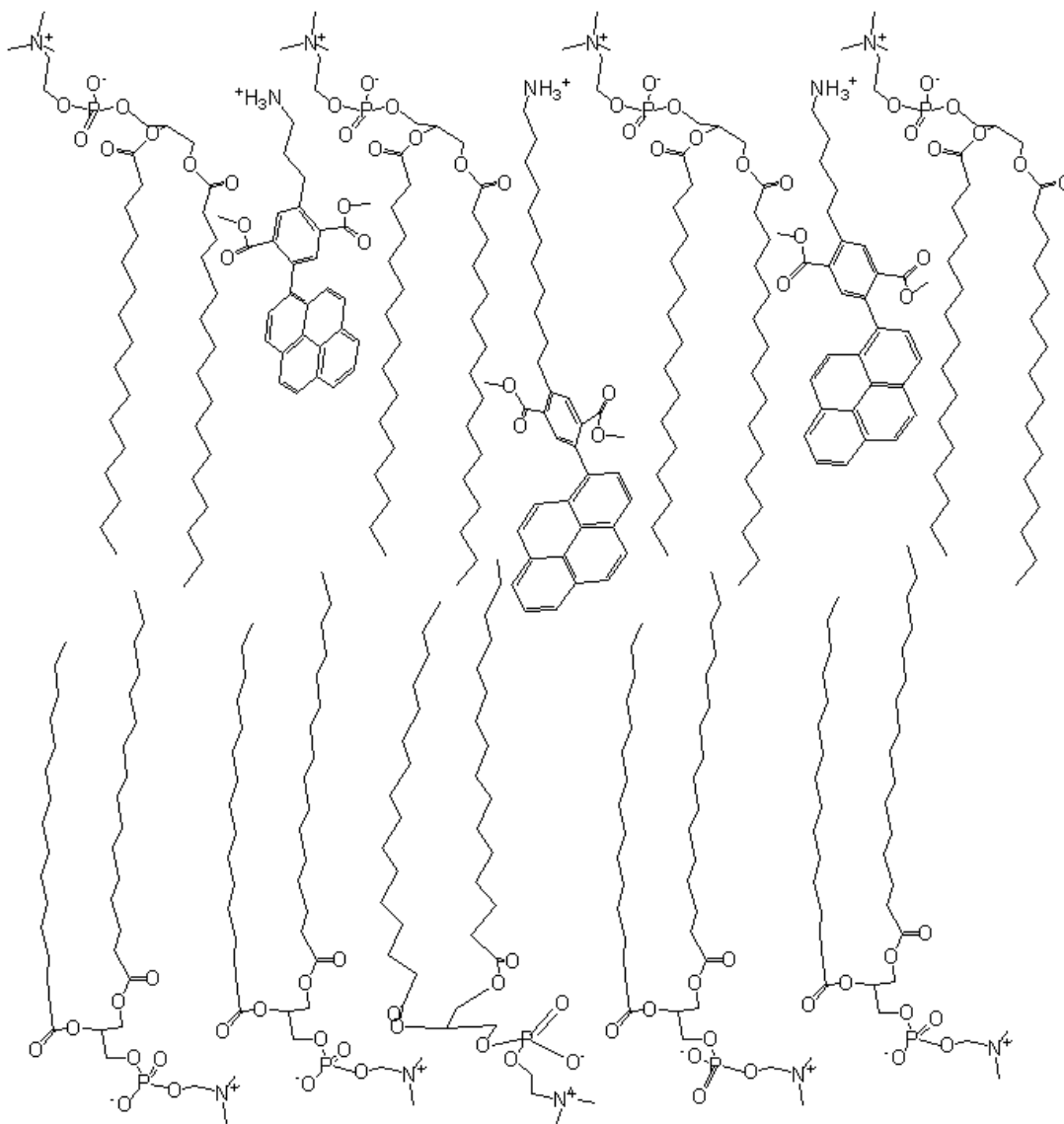


Figure 4.17: Schematic sketch of a DPPC-bilayer with incorporated probes PA3, PA11 and PA5 (from left to right). The bilayer thickness in the liquid crystalline state is around 0.4 nm [73]. The structures shown are the results of AM1 semiempirical calculations and, in the case of DPPC, represent different minimisation minima.

Table 4.3: UV-Vis absorption and fluorescence measurements, parameters and mean lifetimes at emission maxima (using Equation 3.27) of PA3, PA5 and PA11 incorporated in DPPC-vesicles.

Probe	$\nu_{abs}^{max}/10^3 cm^{-1}$	$\nu_f^{max}/10^3 cm^{-1}$	Φ_f^a	$\bar{\tau}/ns$	$k_f/10^7 s^{-1}$	$k_{nr}/10^8 s^{-1}$
PA3	29.053	20.501	0.015	2.34	0.6	4.2
PA5	28.852	20.637	0.041	2.63	1.5	3.6
PA11	28.885	20.473	0.087	2.24	3.8	4.0

^athe error of Φ_f is appr. $\pm 20\%$.

4.2.2 UV/Vis absorption and fluorescence spectra of pyrene-acceptor probes in DPPC-vesicles

The results of steady state fluorescence and UV/Vis absorption measurements of the probes in vesicles are shown in Table 4.3 and in Figure 4.18.

The absorption spectra of the three probes in vesicles are 1 nm to 3 nm redshifted with respect to the absorption spectra of the free probes described in the last section. Small differences between the absorption spectra of PA3, PA5, PA11 and PA3b were seen. The absorption spectra of the free probes in toluene (refractive index $n = 1.5$) against a reference cuvette filled with water ($n = 1.33$) are 4 nm red-shifted with respect to the spectra measured in toluene against a toluene reference cuvette. Since the absorption measurements of the probes incorporated in the vesicles were made with water as reference, it is very likely that the 1 nm to 3 nm shift in the absorption spectra of the probes in the DPPC-vesicles with respect to those of the free probes result from the differences between the refractive index of the DPPC-bilayer ($n_{bulk} = 1.46$ [74]) and of water. Assuming a different refractive index in different regions of the lipid bilayer, the differences in the absorption spectra of the probes could be explained, provided that the probes are incorporated in the bilayer in accordance to Figure 4.17. To our knowledge, quantitative data about differences in the refractive index in different regions of a lipid bilayer has not yet be published.

The fluorescence spectra of PA3, PA5 and PA11 in vesicles show only small differences in shape and maxima but great differences in the fluorescence quantum yield. The spectra are unstructured, have a high Stokes-shift and are wider than the spectra of the free probes in bulk solvents like THF. A slight broadening of the spectra occurs when the probes are measured three to four days after vesicle preparation, as compared to measurements made within 24 h after preparation. The broadening is strongest for PA11. Vesicle decomposition and resulting movement of the probes into different positions in the bilayer may explain the broadening of the spectra after longer storage of the vesicle solution.

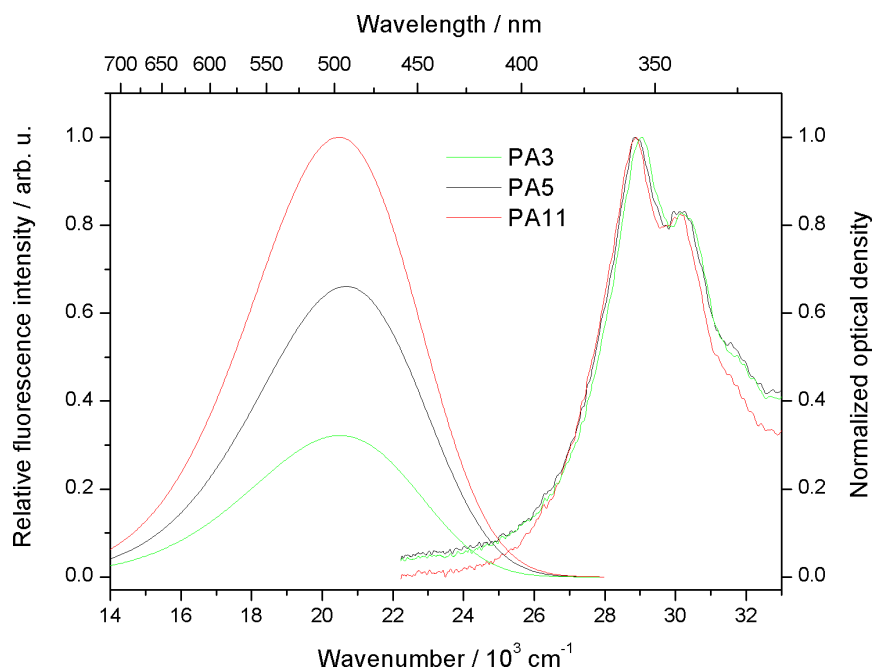


Figure 4.18: Relative fluorescence and UV-Vis absorption spectra of PA3, PA5 and PA11 incorporated in DPPC-vesicles.

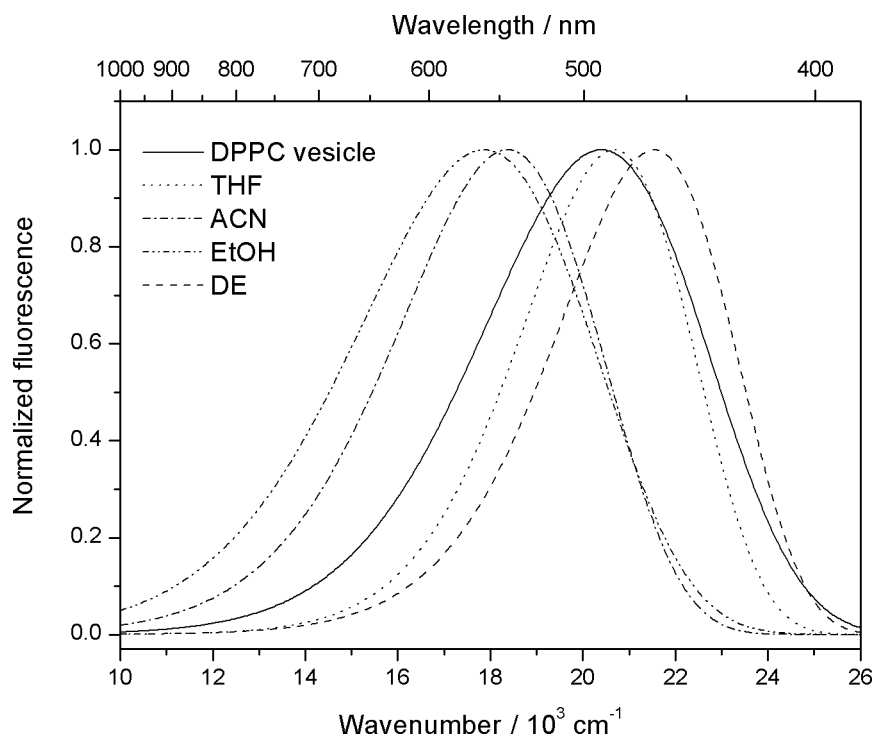


Figure 4.19: Normalised fluorescence spectrum of PA5 in DPPC-vesicles in comparison with the fluorescence spectra of PA5 in solvents of different polarity.

Figure 4.19 shows the fluorescence spectrum of PA5 in DPPC-vesicles in comparison to the fluorescence spectra in solvents of different polarity. The unstructured and red-shifted fluorescence spectrum indicates that an excited state charge transfer occurs in lipid bilayers. The broadening of the fluorescence spectra in vesicles with respect to the spectra in a homogeneous solvent like THF can be explained by considering solvent relaxation (Section 3.3).

The measured spectra of the probes in DPPC-vesicles and in THF show a resemblance in shape and emission maxima to the pyrene excimer spectra. However, Lianos et al. [75] reported that no pyrene excimer formed in 3-sn-phosphatidylglycerol, dipalmitoyl (DPPG) vesicles when the concentrations of DPPG to pyrene were smaller than 100:1. The probes PA3, PA5, PA11 and PA3b did not show a pyrene excimer spectra up to concentrations of $0.5 \cdot 10^{-3}$ Mol in THF. When PA3, PA5 and PA11 were incorporated into DPPC-vesicles with a concentration of DPPC to probe of 250:1, no differences in the shape and position of the fluorescence spectra compared to those with higher probe concentrations could be seen. The formation of excimers can thus be excluded, with high certainty, as the origin of the fluorescence spectra. This may be because the pre-twisted structure of the molecules prevents a close approach of the chromophores.

4.2.3 Fluorescence quantum yields and decay times of the probes in DPPC-vesicles

The time-resolved fluorescence decays of the probes in DPPC-vesicles show multi exponential character. To obtain the mean lifetime $\bar{\tau}$, a three exponential fit and Equation 3.27 was used. The values of Φ_f and $\bar{\tau}$ are listed in Table 4.3. The length of the alkyl chain strongly affects the fluorescence quantum yield but the fluorescence lifetime does not change significantly. In Figure 4.20, the radiative rate constants of PA3, PA5 and PA11 in DPPC-vesicles in comparison with the k_f values in solvents of different polarity are displayed. If the radiative rate constant is used as a measure for the solvent polarity, then it indicates that the environment of PA3 is highly polar. The polarity of the environment of PA5 is lies between the polarity of ACN and BCN and the polarity of the environment of PA11 is comparable to that of THF. The nonradiative rate constants are almost the same for all three probes. The quantum yield can only be calculated with an uncertainty of 20% because the optical density of the probes in vesicles is influenced by a slight but non-reproducible degree of turbidity of the vesicle solution. The multi exponential fluorescence decay can be explained considering that the solvent relaxation time in lipid bilayers is in the same order as the fluorescence lifetime of the probes (Sections 3.3).

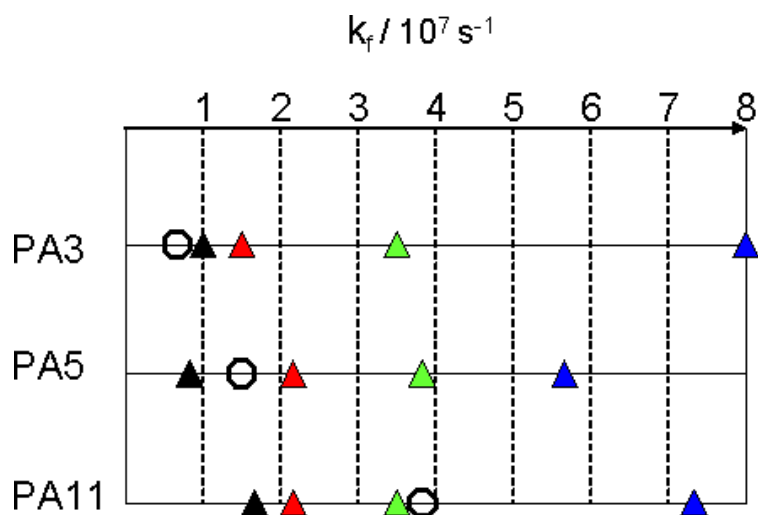


Figure 4.20: Comparison of k_f in bulk solvents (triangles; black for BCN, red for ACN, green for THF and blue for DE) to k_f in DPPC-vesicles (empty circles).

4.2.4 Temperature effects

The temperature dependence of the fluorescence intensity of the probes was a first test for the probes sensitivity to the state of the DPPC-bilayer. The fluorescence intensity of fluorescence probes in bilayers was shown to be highly dependent on the temperature and state of the bilayer [76]. Figure 4.21 shows a steep decrease of the fluorescence intensity after the temperature increased through the main phase transition temperature of DPPC-bilayers. An increase in the fluorescence intensity occurs in the region of the sub-phase transition of DPPC-bilayers. The slope after the main phase transition temperature differs between the probes and is highest for PA3. The measurements imply that the probes are in contact with the interior of the DPPC-vesicles and that the interactions of the probes with the bilayer have the same character (decrease at high temperature, increase during sub phase transition) but are distinguishable (different slopes). The measurements show that the fluorescence of the probes is highly sensitive to the state of the bilayer.

4.3 Solvent relaxation

The method of spectral reconstruction as described in Section 3.3 allows conclusions about the microviscosity of the probes' environment. Figure 4.22 shows the differences in the lifetime decays of PA5 in THF and in vesicles at emission wavelengths of 450 nm and 590 nm. The residues for both wavelengths are calculated using the fit parameters of the decay at shorter wavelengths. No differences in the decays in THF are seen, whereas the decays

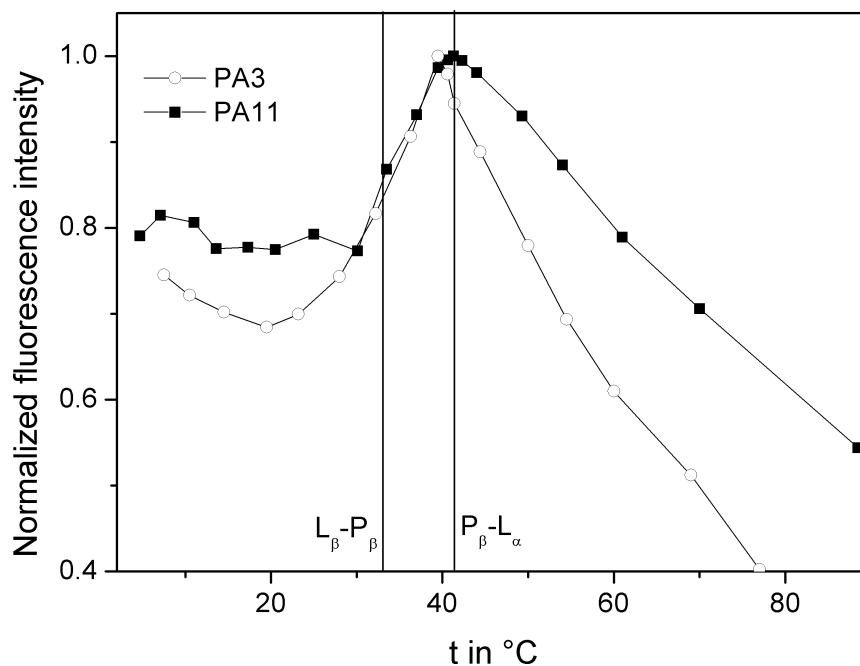


Figure 4.21: Fluorescence intensity of PA3 and PA11 in DPPC-vesicles as a function of temperature. The vertical lines mark the main phase and the sub phase transition temperature.

at different emission wavelengths differ strongly when they are measured in vesicles. These differences in the fluorescence decays are the result of solvent relaxation occurring in a time scale in the order of the fluorescence decay time of the probes and they allow the calculation of the time resolved fluorescence spectra.

4.3.1 Spectral reconstruction

To obtain the reconstructed spectra, the time-resolved fluorescence decays of PA3, PA5 and PA11 incorporated in DPPC-vesicles were measured at eighteen different wavelengths, spanning the steady state fluorescence spectra of the three probes. Each decay was fitted to a sum of three exponentials. The resulting $D(\lambda, t)$ and the steady state fluorescence spectra S_0 were then used to calculate the reconstructed spectra $S(\lambda, t)$ according to Equation 3.41. The results are shown in Figures 4.24, 4.25 and 4.23. The time resolved emission spectra (TRES) of PA3, PA5 and PA11 show a strong time dependence for times shorter than approximately 3 ns. At times longer than approximately 5 ns after excitation, only small changes in the shape and peak position of the TRES occur.

Figure 4.27 shows the time-resolved emission maxima of PA3, PA5 and PA11. The transient red shift of the emission maxima of PA3 is higher than

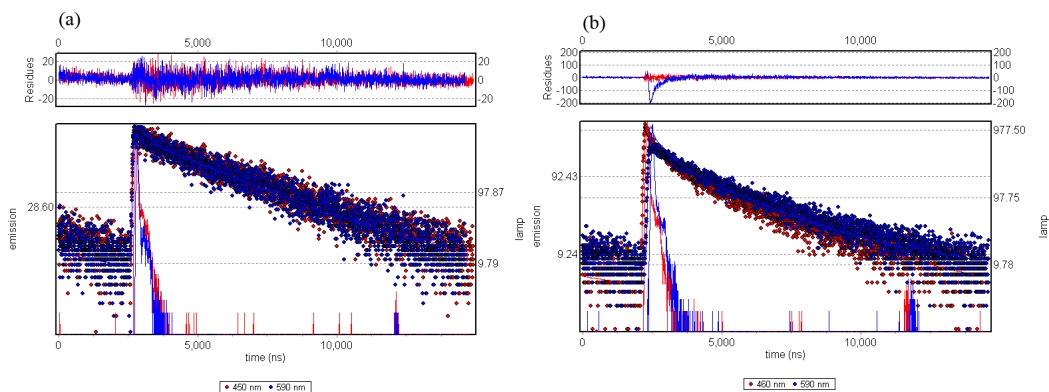


Figure 4.22: Comparison of the fluorescence decays of PA5 in THF (a) and in DPPC-vesicles (b) measured each at two different emission wavelengths. The decay was fitted at the shorter wavelength and the obtained parameters were used to calculate the residua for both wavelength to reveal the differences of the decays at different wavelength.

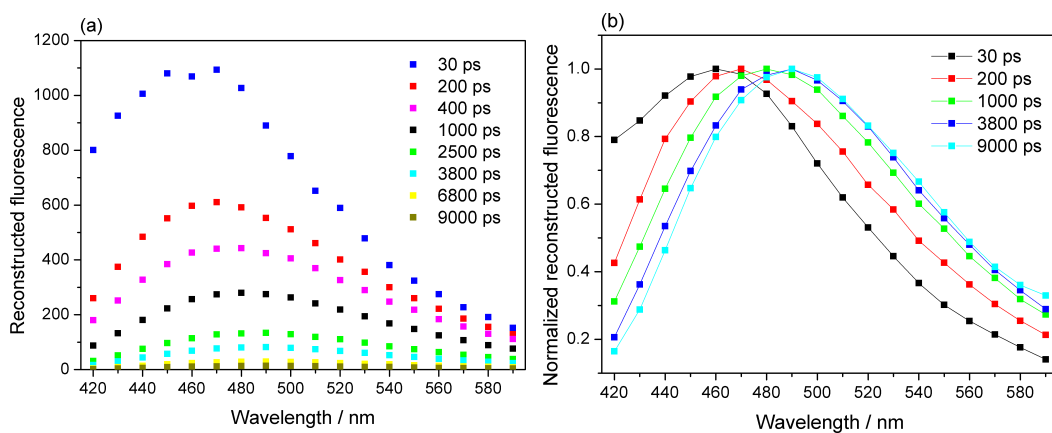


Figure 4.23: Reconstructed fluorescence intensities of PA3 in DPPC-vesicles (a) and normalised reconstructed fluorescence intensities of PA3 in DPPC-vesicles (b).

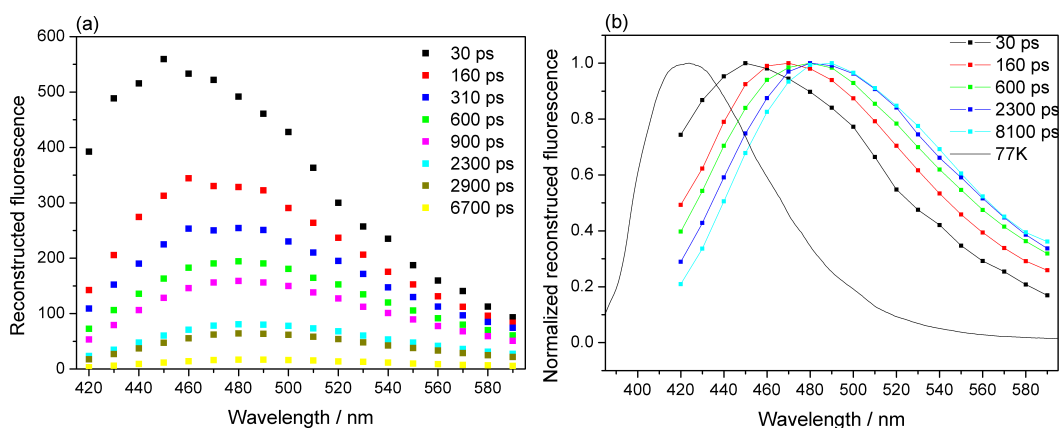


Figure 4.24: Reconstructed fluorescence intensities of PA5 in DPPC-vesicles (a) and normalised reconstructed fluorescence intensities of PA5 in DPPC-vesicles in comparison with the steady state spectra of PA5 in a glass matrix of a DE-EtOH mixture at 77 K (b).

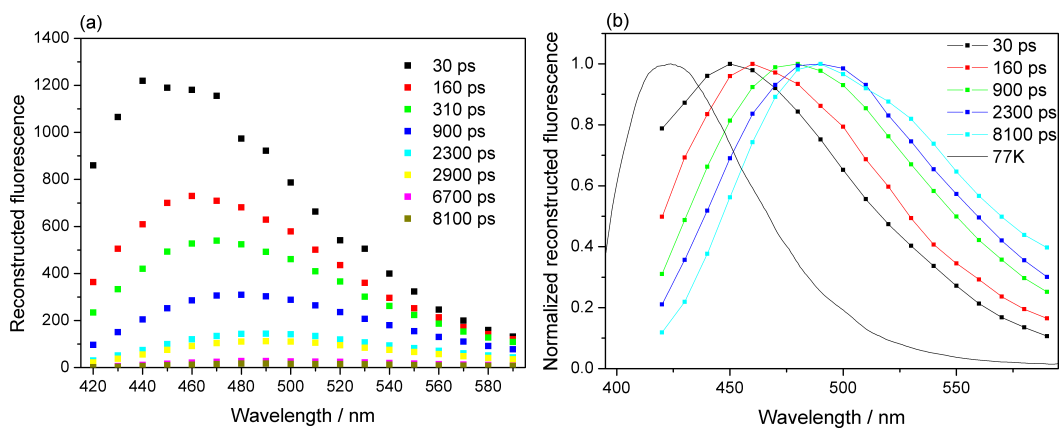


Figure 4.25: Reconstructed fluorescence intensities of PA11 in DPPC-vesicles (a) and normalised reconstructed fluorescence intensities of PA11 in DPPC-vesicles in comparison with the steady state spectra of PA11 in a glass matrix of a DE-EtOH mixture at 77 K (b).

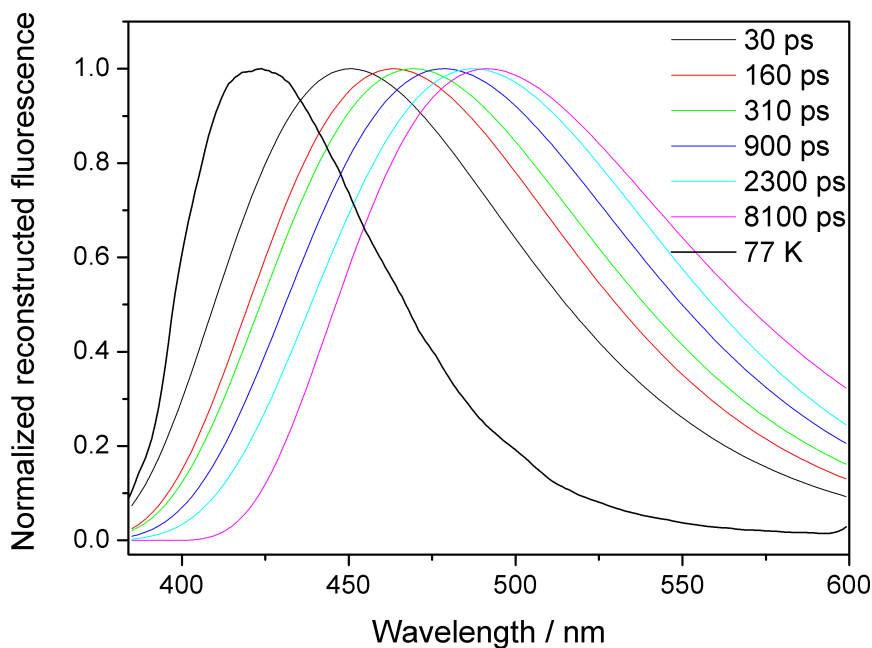


Figure 4.26: Reconstructed spectra of PA11 in DPPC-vesicles after fitting of the data from Figure 4.23 with a log-normal-fit in comparison with spectra of PA11 in a glass matrix of a DE-EtOH mixture at 77 K.

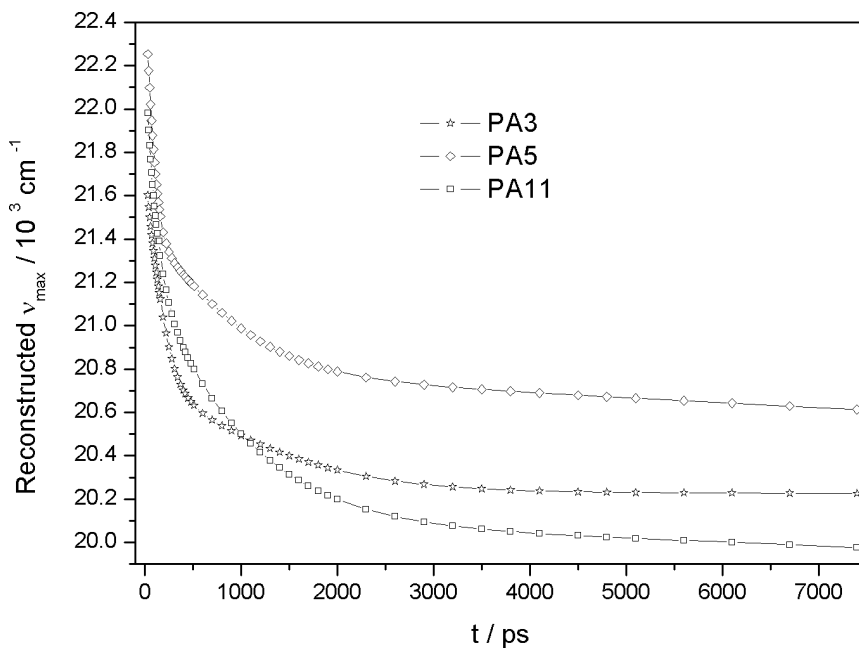


Figure 4.27: Time-resolved emission maxima of PA3, PA5 and PA11.

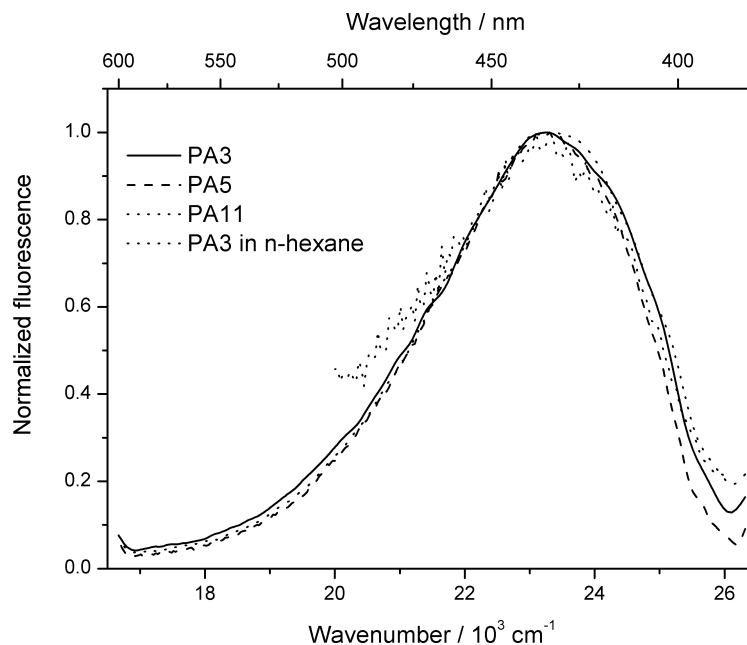


Figure 4.28: Fluorescence spectra of PA3, PA5 and PA11 in a glass matrix of a DE-EtOH mixture at 77 K. The light dotted line shows the fluorescence spectrum of PA3 in n-hexane.

that of PA5, indicating that the polarity of the surrounding of PA3 is higher than that of the surrounding of PA5. The highest transient red shift is seen for PA11, which was assumed to be located close to the center of the bilayer, where the polarity should be lowest. However, the high values for the red shift of PA11 could indicate that backfolding takes place as it was reported for 16AP (Figure 3.11) [65], where an unexpectedly large red shift was also reported. At this time this red shift is not fully understood, but it is thought that the alkyl chain is folding back toward the lipid-water interface [77].

4.3.2 Time-zero estimation

To obtain quantitative information about the solvent relaxation process, it is important to know the time-zero spectrum. The limited time resolution of the experimental setup does not allow the direct measurement of this spectra. It was shown that the time resolution of the experiment greatly influences the obtained time-zero spectrum [36]. Therefore the method described by Maroncelli and Fee is used for a better estimation of the time-zero spectrum [36]: the non-polar fluorescence spectrum provides a good approximation for the time-zero spectrum in a polar solvent. The time-zero spectrum can be observed directly in a glass matrix of a frozen solvent [36]. Figure 4.28 shows the fluorescence spectra of PA3, PA5 and PA11 in a glass matrix of a frozen DE-EtOH

Table 4.4: Emission maxima of PA3, PA5 and PA11 in a glass matrix of a DE-EtOH mixture at 77 K and in n-hexane.

Solvent	PA3	PA5	PA11
DE-EtOH (77 K)	420 nm ^a	423 nm	423 nm
n-hexane	426 nm	429 nm	430 nm

^aemission maxima were obtained after fitting of the measured spectra with PeakFit[®] [78].

mixture and the fluorescence spectrum of PA3 in n-hexane. All spectra were fitted with PeakFit[®] and their emission maxima are given in Table 4.4. In [13] it was reported that the charge transfer state of 2,5E-PP could be frozen out in the non-polar solvent methylcyclohexane at 77 K and a high structured fluorescence from the LE state occurred. The fluorescence spectra of PA3, PA5 and PA11 in a glass matrix of a DE-EtOH mixture are not structured and slightly blue shifted with respect to the fluorescence spectra in n-hexane. Thus we can assume that they can be treated as the "true" time-zero spectra emitted from an already formed charge transfer state, but before any solvent relaxation occurs.

4.3.3 Time-resolved full width at half maximum

Section 3.3 describes how the time evolution of the FWHM allows conclusions about the extent of the observed solvent relaxation. In Figures 4.29, 4.30 and 4.31, the time evolution of the FWHM of PA3, PA5 and PA11 are shown. For PA3 and PA5, the FWHM reach maximum and then decrease, thus indicating that the whole relaxation process is monitored [28]. The time evolution of the FWHM of PA11 also shows an increase followed by an decrease, but it then increases again. It was shown that the time evolution of the FWHM passes a maximum in neat solvents and supercooled liquids [79]. It was further proven that the broadening occurs because every particular fluorophore has a different solvation shell and each solvation shell responds differently to the change in the local electric field after photoexcitation [27, 80, 81]. The FWHM is therefore a measure for the heterogeneity of the probe's microenvironment. A possible explanation for the increase in the FWHM of PA11 is a backfolding of the alkyl chain toward the water-lipid interface of the DPPC-vesicle. The high excited state dipole moment of the probes might force the excited chromophores toward the polar lipid-water interface, resulting in varied positioning in the lipid bilayer of the chromophores and thus in increasing heterogeneity of the chromophores' environment. A backfolding of the alkyl chain is more likely for long chains due to lower sterical hindrances, which would explain why only PA11, the longest probe, shows increasing FWHM.

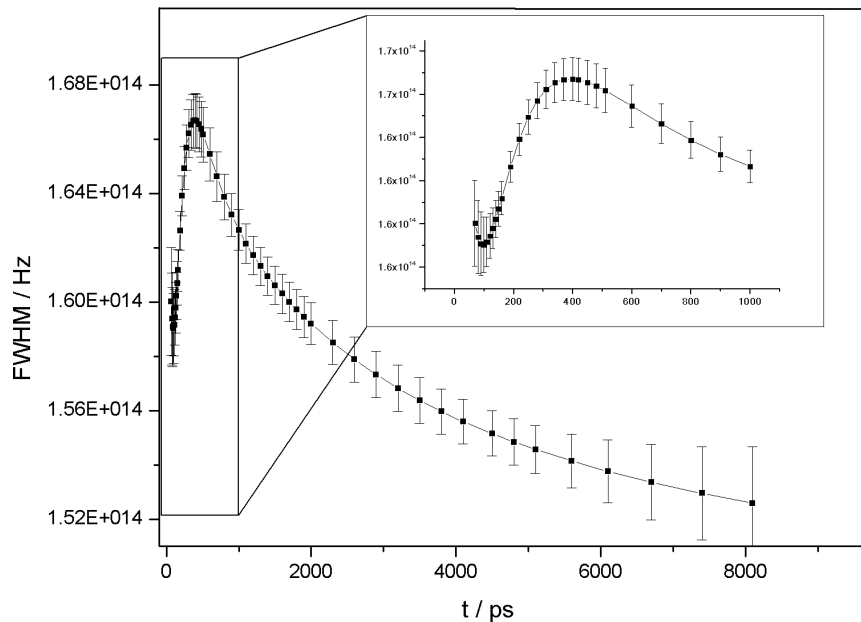


Figure 4.29: Time evolution of FWHM of PA3 in DPPC-vesicles at room temperature (gel phase). The error bars were generated by PeakFit[®] during the fitting of the reconstructed spectra.

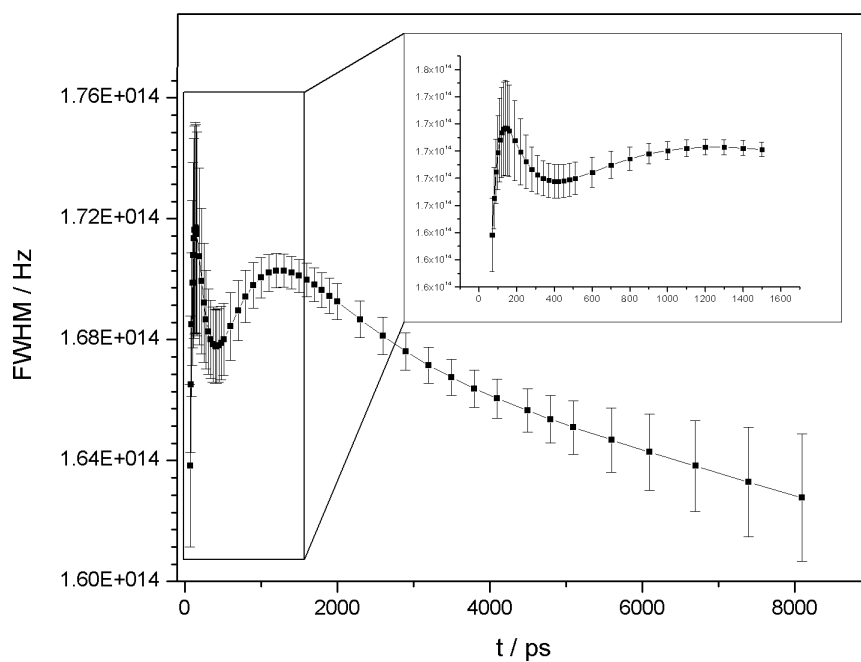


Figure 4.30: Time evolution of FWHM for PA5 in DPPC-vesicles at room temperature (gel phase).

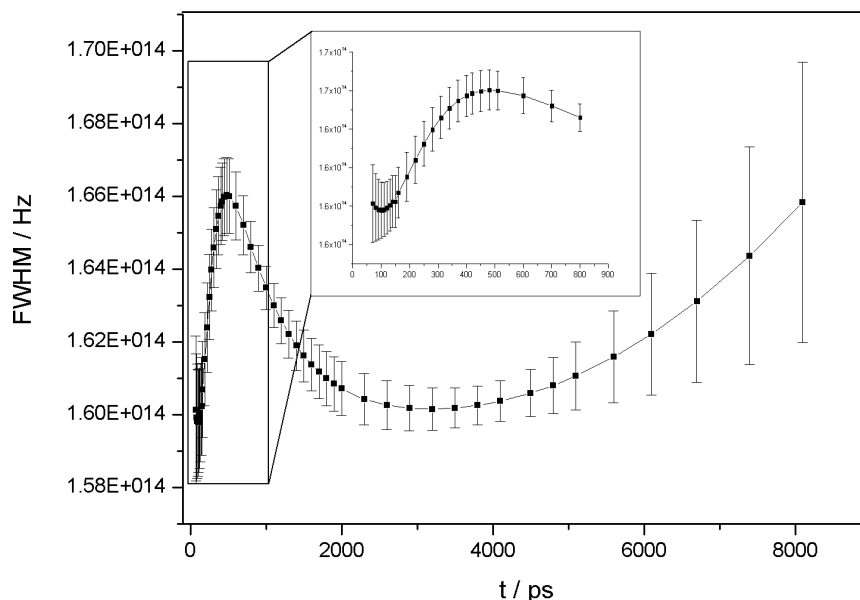


Figure 4.31: Time evolution of FWHM for PA11 in DPPC-vesicles at room temperature (gel phase).

The FWHM of PA5 show an unusual decrease at initial times. In [28] a similar effect was reported for a dye localised in the headgroup region of a DPPC-bilayer in the gel phase. It was assumed that partial localisation of the dye takes place because of a close packing of the bilayer.

4.3.4 Spectral response function

In the previous section, the time-zero spectra were obtained by measuring the fluorescence spectra of the probes in a glass matrix of frozen solvent. The emission maxima of the time-zero spectra allow the calculation of $C(t)$. The spectral response functions for PA3, PA5 and PA11 are shown in Figure 4.32. Table 4.5 lists the solvent relaxation parameters of PA3, PA5 and PA11 in DPPC-vesicles determined at room temperature. The $\nu(\infty)$ values were determined by inspecting the time-resolved emission spectra [79]. The solvent relaxation times of PA3 and PA5 differ by a factor of two, which indicates that the mobility of water molecules is higher in the environment of PA3 than in the environment of PA5. Because the mobility of water molecules decreases toward the center of the lipid bilayer, it can be assumed that PA5 is located closer toward the center of the bilayer than PA3. This is in agreement with the time-resolved emission maxima. The polarity of the bilayer decreases toward the center and thus a blue shifted emission from molecules located close to the center is expected [28]. The solvent relaxation time of PA11 is only slightly higher than that of PA5 but at times smaller than 2 ns the slope of $C(t)$ of

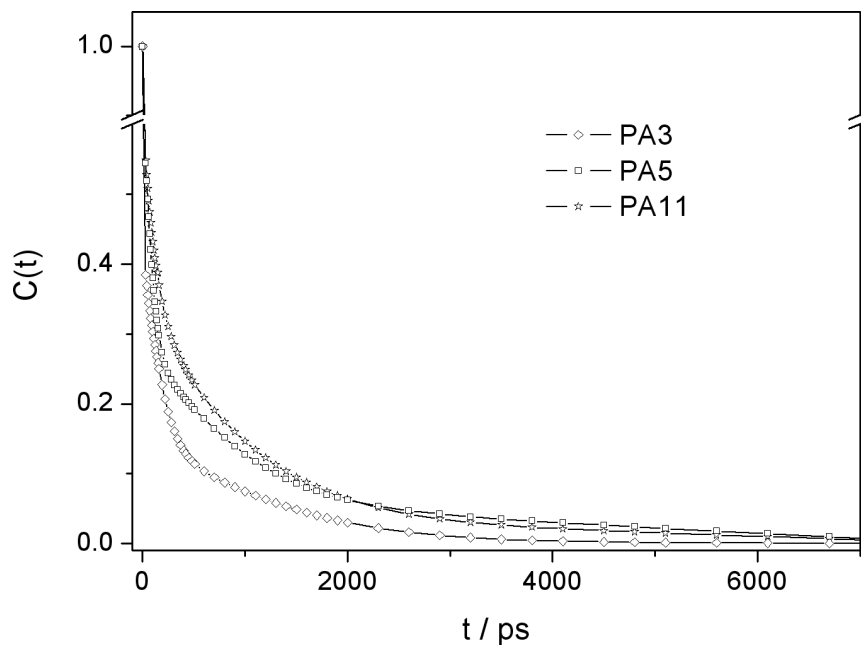


Figure 4.32: Spectral response function of PA3, PA5 and PA11 in DPPC-vesicles at room temperature (gel phase). The area under the curve is a measure for the solvent relaxation time.

Table 4.5: Solvent relaxation parameters of PA3, PA5 and PA11 in DPPC-vesicles at room temperature (gel phase). $\Delta\nu$ is the time-dependent Stokes shift with $\Delta\nu = \nu(0) - \nu(\infty)$. The relaxation times τ_1 , τ_2 and τ_3 are obtained by three exponential fitting of $C(t)$. Note that τ_2 is smaller than the time-resolution of our experiment. Observed SR is calculated by division of $\nu(t = 0 \text{ ps})$ from time-zero estimation and $\nu(t = 80 \text{ ps})$ achieved from TRES measurements.

Compound	$\Delta\nu/cm^{-1}$	τ_1/ps	τ_2/ps	τ_3/ps	$\langle\tau_r\rangle/ps^a$	observed SR (%)
PA3	3600 ± 50	310	0.14	210	240	89
PA5	3000 ± 100	1150	0.5	84	470	90
PA11	3700 ± 100	1100	6	120	490	91

^acalculated using Equation 3.40

PA11 in Figure 4.32 implies that the relaxation process of PA11 is slower than that of PA5. The high red shift of PA11 with respect to PA3 and PA5 implies that PA11 is located closest to the lipid-water interface, but the highest solvent relaxation time implies the opposite: PA11 is incorporated closest to the center of the bilayer. Considering the FWHM of the TRES, it might be assumed that backfolding of the alkyl chain occurs upon photoexcitation of PA11. This hypothesis would explain the high red shift: the backfolding moves the chromophore toward the water-lipid interface and the excited chromophore which emits a photon at later times has a more polar environment and thus emits a photon of lower energy.

The solvent relaxation times of the probes are shorter than those reported for the *n*-(9-anthroyloxy) fatty acids (Section 3.4.2) in DPPC-vesicles in the gel-phase. Possible explanations might include the high probe-to-lipid ratio of around 1:30 and the strong effects of protic solvents. Solvent relaxation measurements at different probe-to-lipid ratios, different temperatures and different phases of the bilayer as well as fluorescence depolarisation measurements, will help to reveal more details about the solvent relaxation processes of the probes in DPPC-bilayers.

4.4 Dye immobilisation and supported bilayers

Molecules incorporated in a vesicle may have a preferential orientation with respect to the bilayer normal. However, if the bilayer is forming a sphere, only the sum of all orientations of incorporated probes will be seen macroscopically. Therefore, vesicles cannot be used to achieve a preferential orientation of charge transfer systems in electric fields. In this section, the first steps to achieve a defined preferential orientation of the probes will be described. The method of vesicle fusion was applied to hydrophilic and functionalised hydrophobic glass slides. In addition, a probe chamber was developed to allow the measurement of fluorescent decay times of immobilised probes on glass supports.

4.4.1 Immobilised fluorophores on a glass support

The measurement of the fluorescence of a single layer of chromophores requires a highly sensitive equipment due to the fact that only a small number of chromophores can be monitored. To develop a probe holder meeting this requirement, the standard dyes pyrenemethylamine (PMA) and rhodamine 110 (Rho110) were covalently attached to glass supports by reaction of the amino groups of the dyes with the epoxy-functionality of the glass supports, which had been functionalised with (3-glycidylpropyl)trimethoxysilane [82]. The results of the surface functionalisation process and the attachment of the

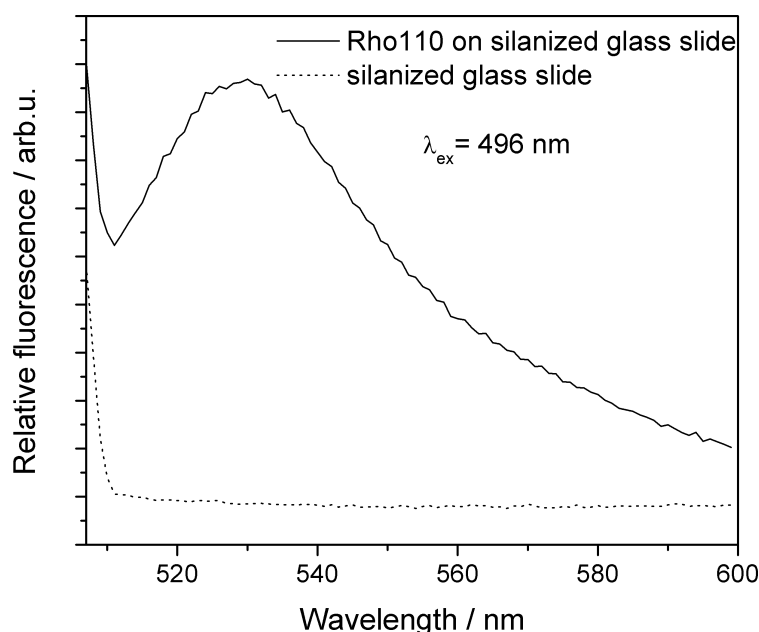


Figure 4.33: Fluorescence spectra of rhodamine 110 covalently bound to a silanised glass slide in comparison to the fluorescence of a blank silanised glass slide.

dyes were characterised using contact angle and AFM measurements. The uncleaned glass slides have a contact angle of $(30 \pm 3)^\circ$. After the cleaning procedure the contact angles are measured to be below 10° : the glass slides are highly hydrophilic. The surface roughness of the clean glass slides was measured using atomic force microscopy to be less than 2 nm. After silanisation with epoxy silanes, the contact angle were measured as $(45 \pm 2)^\circ$, which is in agreement with the contact angles reported for silanised slides in [83]. The surface roughness of the epoxy-silanised layers of about 10 nm measured by atomic force microscopy indicates a formation of polysiloxane layers (Figure 4.35). The contact angle after the attachment of the dyes is $(53 \pm 3)^\circ$.

The probe holder for the glass slides allows the measurement of the emitted light at different positions and angles of the slide with respect to the beam of the incoming excitation light. An angle of 18° off a 45° position of the glass slide toward the excitation light yielded a sufficient emission intensity and a low intensity of scattered light. Figures 4.33 and 4.34 show the fluorescence spectra of PMA and Rho110 after they have been covalently attached to a silanised glass slide in comparison to the fluorescence spectrum of a blank silanised glass slide. The spectra show that a sufficient amount of emitted light can be detected to allow fluorescence measurements. In the fluorescence spectrum of covalently attached PMA, no excimer emission is observed, thus indicating that the chromophores are not highly ordered and closely packed on the sur-

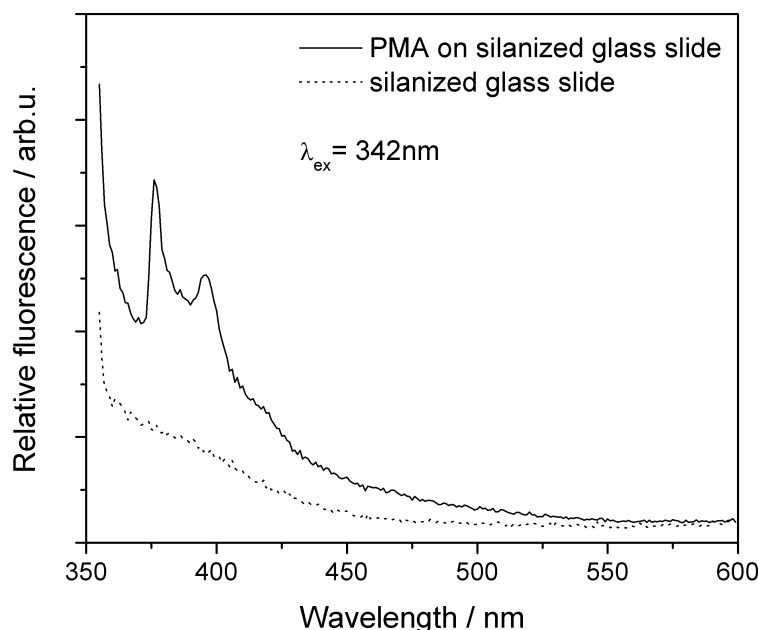


Figure 4.34: Fluorescence spectra of pyrenemethylamine covalently bound to a silanised glass slide in comparison to the fluorescence of a blank silanised glass slide.

face. The photo stability of PMA is very poor and the fluorescence intensity decreases quickly upon illumination. The high photo bleaching threshold of PMA is known, so this is not a surprising effect [84]. Rho110 has a high photo stability and no differences in the fluorescence intensity were found after illumination with laser light for appr. thirty minutes.

The fluorescence lifetimes of PMA and Rho110 on silanised glass slides were measured as (3.0 ± 0.2) ns and (1.0 ± 0.1) ns, respectively. The fluorescence lifetime of Rho110 in methanol was reported to be 4.2 ns [85]. The shorter lifetime of Rho110 on a silanised glass slide can be explained by quenching by oxygen, because the chromophore on the glass slide is directly in contact with air.

4.4.2 Supported DPPC-layers on blank and C₁₂ coated glass slides

Vesicle fusion on hydrophobic and hydrophilic surfaces allows the production of a supported planar lipid bilayer parallel to the supporting material [86]. When a vesicle comes in contact with a hydrophilic or hydrophobic surface it can spread along the surface and form a planar monolayer or bilayer of lipids [49, 51, 56, 87]. However, the stability of fused bilayers is poor and dehydration can change the orientation of the lipids when they are exposed to air [88]. It

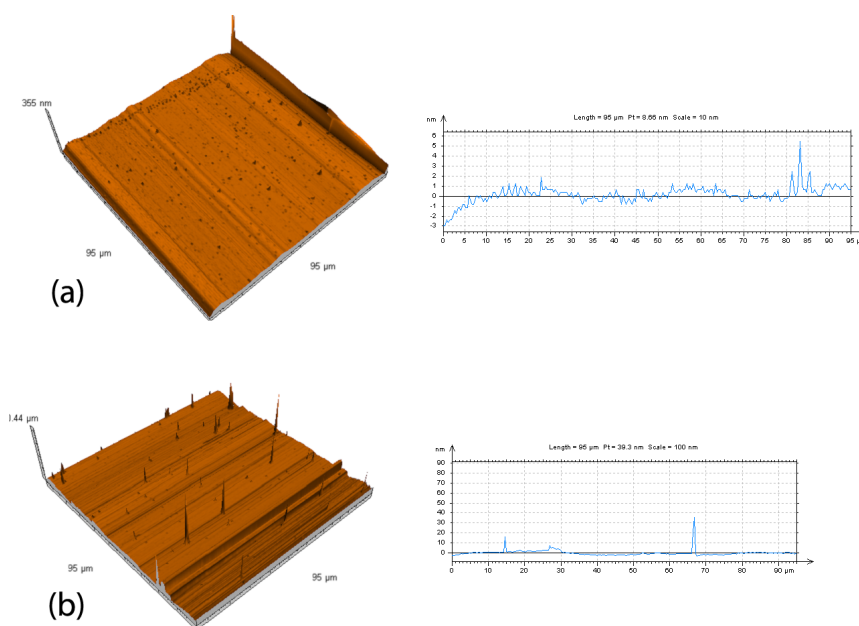


Figure 4.35: AFM pictures of epoxy coated glass slide (a) in comparison to a C₁₂ coated glass slide (b) with corresponding height profiles.

was shown that it can be difficult to obtain large areas of defect-free layers with the method of vesicle fusion [51]. The ionic strength, the pH value and the structure of the substrate surface are factors which highly influence the quality of the obtained lipid layers.

The hydrophilic glass slides were prepared by cleaning untreated glass slides with Deconex[®] 11 Universal solution in a sonicator at 70°C for 30 minutes. The hydrophobic glass slides were prepared by silanisation of clean glass slides with dodecyltrichlorsilane. The silanisation resulted in a contact angle of $(108 \pm 2)^\circ$. The AFM picture of the C₁₂ coated slides shows a smooth surface interrupted by high peaks (Figure 4.35). It can be assumed that the C₁₂ silanisation also resulted in formation of a polysiloxane layer. To improve the smoothness of the C₁₂ coated slides, the silanisation procedure will need to be modified, for example, by adjusting the solvent polarity, to obtain surfaces of higher quality.

For vesicle fusion, 0.1 M vesicle solutions were prepared in a Tris-HCL buffer with a pH of 7.4 and with varying concentrations of NaCl. The blank, cleaned glass slides and the C₁₂ coated glass slides were immersed in the vesicle solution for 16 h under mild agitation. The slides were then carefully washed and another clean, blank glass slide was placed on top of the layer.

The contact angle measurements of the dried glass slides after vesicle fusion showed only small changes. The contact angle of the C₁₂ coated slides decreased to $(89 \pm 5)^\circ$, and the contact angle of the blank glass slides increased to $(38 \pm 5)^\circ$. The dried C₁₂ slides after vesicle fusion showed macroscopic stain-

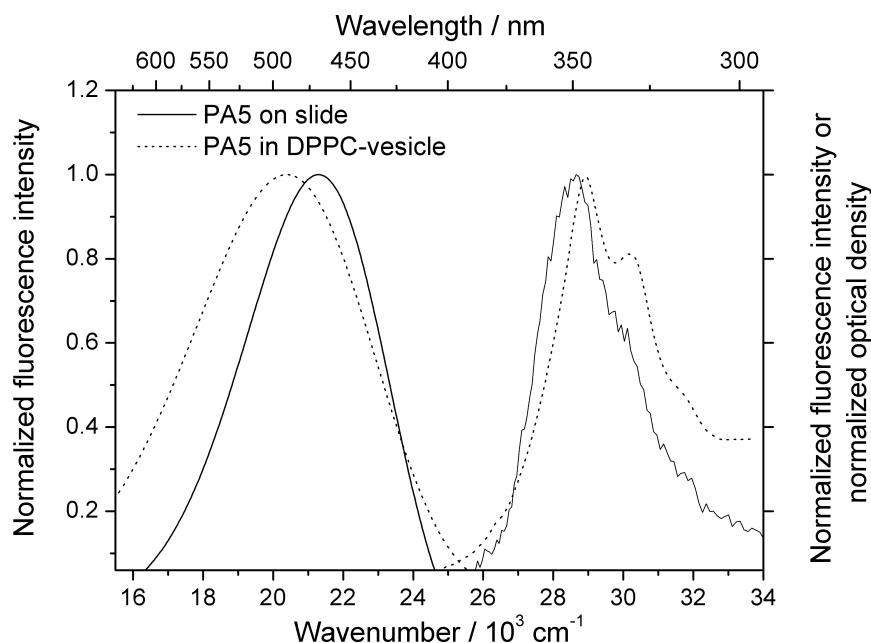


Figure 4.36: Fluorescence and excitation spectra of PA5 on hydrophilic glass slide after fusion of vesicles in comparison to fluorescence and UV/Vis absorption spectra of PA5 incorporated in DPPC-vesicles.

ing. The fluorescence spectra and excitation spectra were measured and can be seen in Figure 4.36. After intense washing of the slides with water, the fluorescence spectra did not change. After rinsing with acetone, no fluorescence spectra could be recorded indicating that the probes were totally removed from the slides. The emission maxima of the probes on slides are blue shifted with respect to the emission maxima of the probes in vesicles. The fluorescent decay times could be recorded with a count rate of up to 5000 counts per second for the blank hydrophilic glass slides after fusion of vesicles. A typical fluorescence decay of PA5 after the procedure of vesicle fusion on a blank glass slide is shown in Figure 4.37.

The mean fluorescence decay time of PA5 in a lipid layer on a glass slide was calculated as 2.57 ns using Equation 3.27 and two exponential fitting of the decay and shows no significant differences from that of PA5 in DPPC-vesicles (2.63 ns).

To interpret the above shown results in more detail, additional experiments to improve the silanisation protocol and the vesicle fusion process are needed. The characterisation of the surfaces with atomic force microscopy and ellipsometry will play an important role.

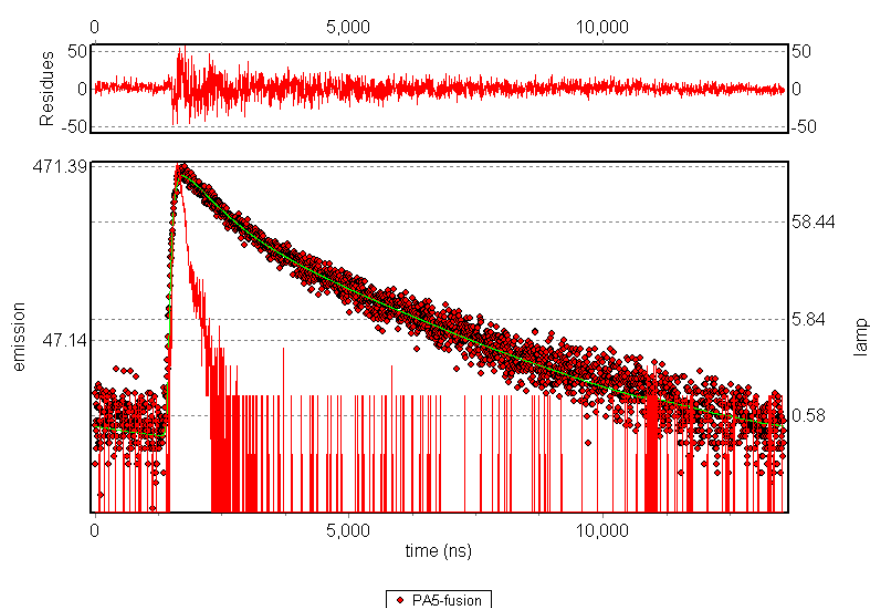


Figure 4.37: Fluorescence decay of PA5 after fusion of DPPC-vesicles onto a hydrophilic glass slide. The decay is fitted with a two exponential decay model using GlobalsWE.

Chapter 5

Experimental Part

5.1 Synthesis of the probes

PA3, PA5 and PA11 were synthesised and purified by Dr. Julia Bricks of the Academy of Science, Kiev and PA3b by Dirk Schubert of ETH-Zürich, all following the method of Suzuki-Miyaura cross coupling described in [89]. The details of the synthesis and the characterisation of the structure of the probes will be published elsewhere.

5.2 UV/Vis absorption and fluorescence measurements

All solvents used for spectroscopic measurements were of spectrophotometric grade. UV/Vis absorption spectra were measured with a ATI UNICAM series spectrometer. For quantum yield measurements, the optical density of the solution was held below 0.1. Fluorescence spectra were measured on a SLM AMINCO-Bowman AB 2 spectrofluorimeter and corrected for instrumental sensitivity. The fluorescence spectra were recorded in the wavelength domain. To obtain the emission maxima, the emission spectra were converted to the wavenumber domain, multiplied by λ^2 [90] and then fitted with a log-normal function in PeakFit[®]. A quinine bisulfate solution ($\Phi_f = 0.52$) in 0.1 M H₂SO₄ was used as a standard for the measurements of the fluorescence quantum yields [91]. Measurements at 77 K were performed in glass tubes immersed in liquid nitrogen. The probes were solved in a mixture of diethylether and ethanol with a ratio of appr. 60:1.

5.3 TC-SPC

Fluorescence decay measurements were performed using the principle of time-correlated single photon counting (TC-SPC) with a setup using a passively mode-locked Ti:sapphire laser from SpectraPhysics pumped by a Millennia pro diode-pumped, CW visible laser system. Pulse duration is appr. 80 fs and pulse frequency is appr. 81 MHz. Two polarizers at 54.7° to each other were used: one between the excitation source and the probe, the other between the probe and the detector. The excitation wavelength was obtained by second harmonic generation from the fundamental wavelength of 700 nm. Fluorescence and scatter were detected by a microchannel plate photomultiplier (MCP, Hamamatsu R 1564 U-01 at -30°C) coupled by a quartz fiberoptic to the emission monochromator (Oriel MS257). The signal from a constant fraction discriminator (CFD, Tennelec 454) was used as the start pulse for the time to amplitude converter (TAC, Tennelec TC864) operating in reverse mode. Stop pulses were obtained by imaging a small part of the excitation light with a photodiode (HSA-X-S-1G4-SI, FEMTO[®] Messtechnik GmbH). The MCP pulses were amplified using a Hamamatsu C4890 wide band amplifier. The count rate was held below 6k counts per second to avoid pile-up effects. A multichannel analyzer (Fast Comtec MCDLAP) was used for data accumulation. The instrument response function was detected using a stray solution at excitation wavelength and has width of 60-70 ps. The program Globals Unlimited [92] was used for the analyses of the fluorescence decays. Each recorded decay consisted of 230k to 280k counts. The error of the lifetimes is appr. 5%.

5.4 Vesicle preparation

1,2-Dipalmitoyl-sn-glycero-3-phosphocholine (DPPC) in chloroform was purchased from Avanti[®] Polar Lipids Inc. and used without further purification. The probes were added to the DPPC-chloroform solution to yield a lipid-to-probe ratio of 30:1. The chloroform was removed in a vacuum evaporator and was then dried under high vacuum for two more hours to remove remaining traces of chloroform. After addition of ultrapure water with a temperature of 50°C , the lipid suspension (1 mM) was sonicated at 50°C for appr. thirty minutes until the solution was clear. The fluorescence, UV/Vis absorption and DLS measurements were performed at room temperature within 24 h after preparation.

5.5 Dynamic light scattering

The average diameter of the vesicles was determined by dynamic light scattering (DLS), using a Zetasizer 3000HS (Malvern Instruments) at a temperature

of $25 \pm 0.1^\circ\text{C}$. The intensity of the laser light scattered by the samples was detected at an angle of 90° with a photomultiplier. The vesicle solutions were diluted with distilled water in order to avoid multiscattering phenomena. For each probe incorporated in vesicles at least three measurements were made. For each of these specimens ten autocorrelation functions were analysed using a cumulative analysis. From this analysis, the z-average value was obtained, which is an approximation of the diameter of the vesicles. Samples were analysed within 24 h after preparation.

5.6 Glass slide preparation

Glass slides used in this work were NexterionTM Glass B slides (Schott). Before further usage they were cleaned in Deconex[®] 11 Universal solution (Borer Chemie) in a sonicator at 70°C for 30 minutes. The slides were dried under a stream of nitrogen and then used within ten minutes after cleaning.

For silanisation, the slides were placed in a 2.5% solution of (3-glycidylpropyl)trimethoxysilane (FLUKA) in toluene at 80°C for three hours. They were rinsed then four times with methanol, twice with acetone and then washed once with acetone. For thermal curing, they were then placed in an oven at 100°C for at least fifteen hours. Until further usage they were stored under an atmosphere of dry nitrogen. C₁₂ coated glass slides were prepared using the same steps, except with dodecyltrichlorosilane (ABCR GmbH) replacing (3-glycidylpropyl)trimethoxysilane.

Pyrenemethylamine and rhodamine 110 were purchased from Aldrich. For covalent attachment of the dyes, the silanised glass slides were kept for two hours in a 10 mM solution of the dyes in ethylenglycol at 90°C for two hours. Then they were rinsed four times with acetone and twice with deionised water and placed for one hour in deionised water. Contact angle measurements were made after each step and fluorescence was measured within 24 h after preparation.

5.7 Contact angle measurements

Contact angles of 3 μl drops of ultrapure water were measured with a contact angle measurement setup (OCA 15 plus, dataphysics) using the sessile drop method. Contact angles were measured at ten or more different positions of the glass slide.

5.8 Atomic force microscopy

Atomic force microscopy (AFM) measurements on glass slides were made with a Nanosurf MobileS Rasterkraft Mikroskop System from Nanosurf AG with a cantileva NCLR-10 Pointprobe[®]-Silizium SPM sensor in non-contact mode.

5.9 Vesicle fusion

Hydrophobic (C₁₂ coated) and hydrophilic (blank, cleaned) glass slides were prepared as described above. For vesicle fusion experiments, vesicle solutions as described above were prepared in a TRIS-HCl buffer at pH 7.4 with several different concentrations of up to 100 mM NaCl instead of ultrapure water. The glass slides were then placed in the vesicle solutions under mild agitation overnight.

Chapter 6

Summary

A set of four fluorescence probes (PA3, PA5, PA11 and PA3b) was synthesised for this work. Each consist of a pyrene-acceptor moiety, an alkyl chain (with different length for each probe) and an ionic group at the end of the alkyl chain.

In the first part of this work, the photophysical behaviour of the probes was measured in homogeneous solvent environments. The UV/Vis absorption and the fluorescence spectra of the probes were measured in solvents of different polarity. The positions of the absorption maxima of the probes were found not to be dependent on the solvent polarity. This can be explained by the low ground state dipole moments of the probes, which were calculated with with AM1 semiempirical calculations to be 3.5 D, 3.5 D and 3.3 D for PA3, PA5 and PA11, respectively.

The fluorescence spectra of the probes are unstructured and red shifted, with respect to the fluorescence spectrum of the parent chromophore PhP. The Stokes-shifts of the fluorescence spectra of the probes increase with increasing solvent polarity. The shifts in the emission maxima were used to calculate the excited state dipole moments of the probes, using a modified form of the Lippert-Mataga equation which considers that the fluorescence occurs from an excited state different from the LE state. The high excited state dipole moments (appr. 21 D for all three probes) in comparison with the small ground state dipole moments indicate that the probes form a charge transfer state upon photoexcitation.

The quantum yields and fluorescence decay times of the probes in solvents of different polarity were measured, allowing the calculation of the radiative and nonradiative rate constants and the fluorescence transition dipole moments. The radiative rate constants and the fluorescence transition dipole moments were found to decrease with increasing solvent polarity. This can be explained by further twisting between the acceptor moiety and the donor moiety of the molecules. The solvent polarity was found to have only small effects

on the nonradiative rate constants. The differences between the structures of the probes were found to have only slight influences on their photophysics.

Ethanol, as a protic solvent, was found to have a significant effect on the nonradiative rate constants of the probes. In a water-acetonitrile mixture, it was shown that the nonradiative rate constant increases significantly with increasing water concentration. This effect was further examined using a Stern-Volmer quenching formalism to better understand the effects of aqueous environments on the probes before further work in vesicles, which also represent an aqueous environment. It was shown that water quenches the fluorescence of the probes dynamically and that the quenching efficiency was decreased when the accessibility of the acceptor moiety to water molecules was lowered. A modified Stern-Volmer plot was used to quantify the quenching efficiency.

In the second part of this work, the three probes PA3, PA5 and PA11, were incorporated in lipid bilayers in the form of DPPC-vesicles. The UV/Vis absorption spectra of the incorporated probes show a 3 nm red shift with respect to the absorption spectra of the probes in bulk solvents. This effect could be explained by considering the different refractive indices of the lipid bilayer and reference cuvette.

The fluorescence spectra of the probes in vesicles are structureless, with emission maxima close to those in THF. The red shift and the structureless fluorescence spectra imply that the probes form an excited charge transfer state upon photoexcitation. The fluorescence spectra in DPPC-vesicles are broadened in comparison with the fluorescence spectra in bulk solvents.

The quantum yields and fluorescence decay times in DPPC-vesicles were measured and used to calculate the radiative and nonradiative rate constants. The fluorescence quantum yields differ significantly for the three probes whereas the fluorescence decay times differ only slightly. Decays measured in DPPC-vesicles show a multi exponential decay behaviour in contrast to the decays measured in bulk solvents of low viscosity. The radiative rate constants of the probes decrease with decreasing length of the alkyl chain. The nonradiative rate constants show no dependence on the length of the alkyl chain.

The broadening of the fluorescence spectra and the multi exponential fluorescence decay behaviour can be explained by considering solvent relaxation processes that occur in a time scale close to that of the fluorescence lifetime. The differences in the radiative rate constants can be explained when the differences in the polarity of the probes' surroundings are considered. The polarity in DPPC-bilayers decreases towards the center of the bilayer and when it is assumed that the probes are located in different depths of the bilayer, the differences in the radiative rate constants can be explained.

The method of spectral reconstruction was applied to the probes incorporated in DPPC-vesicles to obtain more information about the probes position in the bilayer. Fluorescence decays were recorded at eighteen different emis-

sion wavelengths spanning the fluorescence spectra of the probes. Each decay was fitted using a three exponential decay model and the time-dependent fluorescence spectra were calculated. The time-dependent Stokes shifts and the time-resolved FWHM of the probes in DPPC-vesicles were calculated using a log-normal fit of the reconstructed spectra. The time-resolved FWHM show an increase at short times followed by a decrease, indicating that the whole relaxation process is monitored. An increase of the FWHM at longer times was observed for the probe PA11. The overall red shift, which is known to be directly proportional to the polarity function of a solvent, was found to be highest for PA11, followed by PA3 and then PA5.

To obtain quantitative measurements of the solvent relaxation time, the spectral response function was calculated. The time-zero spectra were obtained by measuring the fluorescence spectra of PA3, PA5 and PA11 in a glass matrix of a frozen DE-EtOH mixture. These fluorescence spectra were unstructured and the emission peaks were slightly blue shifted with respect to the fluorescence spectra measured in the non-polar solvent n-hexane and can therefore be treated as the time-zero spectra. The solvent relaxation times of PA3, PA5 and PA11 were calculated to be 240 ps, 450 ps and 480 ps, respectively. The solvent relaxation times reflect the mobility of water molecules surrounding the probes, which decreases toward the center of the bilayer. It was shown that the mobility of surrounding water molecules is highest for PA3, indicating that PA5 and PA11 are positioned closer to the center of the bilayer than PA3.

The solvent relaxation time and the large red shift of the time resolved emission maxima of PA11 compared to those of PA3 and PA5 cannot be understood assuming PA11 is situated in the center of the bilayer, as it would be expected to considering only its structure. Effects like the backfolding of the alkyl chain or an initial incorporation of PA11 at different depths in the bilayer are possible explanations.

Nevertheless, it can be assumed that PA3 and PA5 probe different regions of the lipid bilayer. The high dependence of the fluorescence intensity of the incorporated probes on different temperatures and phases of the lipid bilayer allows a first application of the molecules as fluorescent probes.

In the third part of this work, experimental steps toward providing oriented charge-transfer systems on planar lipid layers on a support are performed. Glass slides were treated to create hydrophilic or hydrophobic surfaces to allow the fusion of vesicles into lipid bilayers or monolayers, respectively. The glass slides were characterized with contact-angle and AFM measurements. A monolayer of Rhodamine 110 was covalently bound to a silanised glass slide and emission intensities sufficient for steady-state and time-resolved fluorescence measurements were recorded. The protocol of the fusion experiment needs to be improved but initial steady-state and time-resolved fluorescence measurements are promising.

Bibliography

- [1] Mathies R. and Stryer L. Retinal has a highly dipolar vertically excited singlet state: Implications for vision. *Proc. Nat. Acad. Sci.*, 73:2169–2173, 1976.
- [2] Ohta N. Electric field effects on photochemical dynamics in solid films. *Bull. Chem. Soc. Jpn.*, 75:1637–1655, 2002.
- [3] Nakabayashi T., Wahadoszamen Md., and Ohta N. External electric field effects on state energy and photoexcitation dynamics of diphenylpolyenes. *J. Am. Chem. Soc.*, 127:7041–7052, 2005.
- [4] Yoshizawa T., Iwaki Y., Osaka N., Nakabayashi T., Zachariasse K. A., and Ohta N. External electric field effects on absorption, fluorescence and phosphorescence spectra of 4-(dimethylamino)benzonitrile in a polymer film. *J. Phys. Chem. B*, 108:19132–19139, 2004.
- [5] Ashwell G. J., Tyrrell W. D., and Whittam A. J. Molecular rectification: Self-assembled monolayers in which donor(-bridge)-acceptor moieties are centrally located and symmetrically coupled to both gold electrodes. *J. Am. Chem. Soc.*, 126:7102–7110, 2004.
- [6] Rehm D. and Weller A. Bindungszustand und fluoreszenzspektren von hetero-excimeren. *Z. Phys. Chem.*, 69:183–200, 1970.
- [7] Kavarnos G. J. and Turro N. J. Photosensitization by reversible electron transfer: Theories, experimental evidence, and examples. *Chem. Rev.*, 86: 401–409, 1986.
- [8] Suppan P. *Chemistry and Light*, The Royal Society of Chemistry, Cambridge, 1994.
- [9] Grabowski Z. R., Rotkiewicz K., and Rettig W. Structural changes accompanying intramolecular electron transfer: Focus on twisted intramolecular charge-transfer states and structures. *Chem. Rev.*, 103:3899–4032, 2003.

- [10] Rettig W. Charge separation in excited states of decoupled systems - tict compounds and implications regarding the development of new laser dyes and the primary process of vision and photosynthesis. *Angew. Chem. Int. Ed. Engl.*, 25:971–988, 1986.
- [11] Zachariasse K. A., von der Haar T., Hebecker A., Leinhos U., and Kühnle W. Intramolecular charge transfer in aminobenzonitriles : requirements for dual fluorescence. *Pure Appl. Chem.*, 65:1745–1750, 1993.
- [12] Rettig W. and Lutze S. Mechanistic considerations for the dual fluorescence of dimethylaminobenzonitrile: a fluorescence anisotropy study. *Chem. Phys. Lett.*, 341:263–271, 2001.
- [13] Weigel W., Rettig W., Dekhtyar M., Modrakowski C., Beinhoff M., and Schlüter A. D. Dual fluorescence of phenyl and biphenyl substituted pyrene derivatives. *J. Phys. Chem. A.*, 107:5941–5947, 2003.
- [14] Maus M., Rettig W., Bonafoux D., and Lapouyade R. Photoinduced intramolecular charge transfer in a series of differently twisted donor-acceptor biphenyls as revealed by fluorescence. *J. Phys. Chem. A.*, 103:3388–3401, 1999.
- [15] Berlman I. B. and Steingraber O. J. Further evidence of a hidden singlet transition in biphenyl. *J. Chem. Phys.*, 43:2140–2141, 1965.
- [16] Strickler S. J. and Berg R. A. Relationship between absorption intensity and fluorescence lifetime of molecules. *J. Chem. Phys.*, 37:814–822, 1962.
- [17] Lakowicz J. R. *Principles of Fluorescence Spectroscopy*, Plenum Press, New York, 1983.
- [18] Thulborn K. R. and Sawyer W. H. Properties and the locations of a set of fluorescent probes sensitive to the fluidity gradient of the lipid bilayer. *Biochim. Biophys. Acta*, 511:125–140, 1978.
- [19] Suppan P. Solvatochromic shifts: the influence of the medium on the energy of electronic states. *J. Photochem. Photobiol. A*, 50:293–330, 1990.
- [20] Lippert E. Spectroscopic determination of the dipole moment of aromatic compounds in the first excited singlet state. *Z. Elektrochem.*, 61:962–975, 1957.
- [21] Kawski A. *Acta Phys. Pol.*, 29:507, 1966.
- [22] Mataga N., Kaifu Z., and Koizumi M. Solvent effects upon fluorescence spectra and the dipole moments of excited molecules. *Bull. Chem. Soc. Jpn.*, 29:465–470, 1956.

- [23] Liptay W. Solvent-dependence of the wave number of electron bands and physicochemical fundamentals. *Z. Naturforsch.*, 20a:1441–1471, 1965.
- [24] Rösch N. and Zerner M. C. Calculation of dispersion energy shifts in molecular electronic spectra. *J. Phys. Chem.*, 98:5817–5823, 1994.
- [25] Ravi M., Soujanya T., Samanta A., and Radhakrishnan T. P. Excited-state dipole moments of some coumarin dyes from a solvatochromic method using the solvent polarity parameter, ent. *J. Chem. Soc. Faraday Trans.*, 91:2739–2742, 1995.
- [26] Mukherjee S., Chattopadhyay A., Samanta A., and Soujanya T. et al. Dipole moment change of nbd group upon excitation studied using solvatochromic and quantum chemical approaches: Implications in membrane research. *J. Phys. Chem.*, 98:2809–2812, 1994.
- [27] Horng M. L., Gardecki J. A., Papazyan A., and Maroncelli M. Subpicosecond measurements of polar solvation dynamics: Coumarin 153 revisited. *J. Phys. Chem.*, 99:17311–17337, 1995.
- [28] Jurkiewicz P., Sýkora J., Olzyska A., Humpolícková J., and Hof M. Solvent relaxation in phospholipid bilayers: Principles and recent applications. *J. Fluorescence*, 15:883–894, 2005.
- [29] Arzhantsev S., Zachariasse K. A., and Maroncelli M. Photophysics of trans-4-(dimethylamino)-4'-cyanostilbene and its use as a solvation probe. *J. Phys. Chem. A*, 110:3454–3470, 2006.
- [30] Arzhantsev S., Ito N., Heitz M., and Maroncelli M. Solvation dynamics of coumarin 153 in several classes of ionic liquids: cation dependence of the ultrafast component. *Chem. Phys. Lett.*, 381:278–286, 2003.
- [31] Ingram J. A., Moog R. S., Ito N., Biswas R., and Maroncelli M. Solute rotation and solvation dynamics in a room-temperature ionic liquid. *J. Phys. Chem. B*, 107:5926–5932, 2003.
- [32] Ito N., Arzhantsev S., Heitz M., and Maroncelli M. Solvation dynamics and rotation of coumarin 153 in alkylphosphonium ionic liquids. *J. Phys. Chem. B*, 108:5771–5777, 2004.
- [33] Ware W. R., Lee S. K., Brant G. J., and Chow P. P. Nanosecond time-resolved emission spectroscopy: Spectral shifts due to solvent-excited solute relaxation. *J. Chem. Phys.*, 54:4729–4737, 1971.
- [34] Ware W. R., Chow P., and Lee S. K. Time-resolved nanosecond emission spectroscopy: spectral shift due to solvent-solute relaxation. *Chem. Phys. Lett.* 2, pages 356–358, 1968.

- [35] Chakrabarti S. K. and Ware W. R. Nanosecond time-resolved emission spectroscopy of 1-anilino-8-naphthalene sulfonate. *J. Chem. Phys.*, 55: 5494, 1971.
- [36] Fee R. S. and Maroncelli M. Estimating the time-zero spectrum in time-resolved emission measurements of solvation dynamics. *Chem. Phys.*, 183:235–247, 1994.
- [37] Gunstone F. D., Harwood J. L., and Padley F. B. *The Lipid Handbook*, 2nd edition, Chapman and Hall, Cambridge, 1994.
- [38] van Doren H. A., Smits E., Pestman J. M., Engberts J. B. F. N., and Kellogg R. M. Mesogenic sugars. from aldoses to liquid crystals and surfactants. *Chem. Soc. Rev.*, 29:183–199, 2000.
- [39] Koynova R. and Caffrey M. Phases and phase transitions of the phosphatidylcholines. *Biochim. Biophys. Acta*, 1376:91–145, 1998.
- [40] Nagle J. F. and Tristram-Nagle S. Structure of lipid bilayers. *Biochim. Biophys. Acta*, 1469:159–195, 2000.
- [41] Chapman D., Williams R. M., and Ladbroke B. D. Physical studies of phospholipids: Vi. thermotropic and lyotropic mesomorphism of some 1,2-diacylphosphatidylcholines (lecithins). *Chem. Phys. Lipids*, 1:445–475, 1967.
- [42] Ringsdorf H., Schlarb B., and Venzmer J. Molecular architecture and function of polymeric oriented systems: Models for the study of organization, surface recognition, and dynamics of biomembranes. *Angew. Chem. Int. Ed. Engl.*, 27:113–158, 1988.
- [43] Bangham A. D., De Gier J., and Greville G. D. Osmotic properties and water permeability of phospholipid liquid crystals. *Chem. Phys. Lipids*, 1: 225–246, 1967.
- [44] Huang C. Phosphatidylcholine vesicles: Formation and physical characteristics. *Biochemistry*, 8:344–352, 1969.
- [45] Suurkuusk J., Lentz B. R., Barenholz Y., Biltonen R. L., and Thompson T. E. A calorimetric and fluorescent probe study of the gel-liquid crystalline phase transition in small, single-lamellar dipalmitoylphosphatidylcholine vesicles. *Biochemistry*, 15:1393–1401, 1976.
- [46] Huang C. and Thompson T. E. Preparation of homogeneous, single-walled phosphatidylcholine vesicles. *Methods Enzymol.*, 32:485–489, 1974.

- [47] Hubbard J. B., Silin V., and Plant A. L. Self assembly driven by hydrophobic interactions at alkanethiol monolayers: mechanisms of formation of hybrid bilayer membranes. *Biophys. Chem.*, 75:163–176, 1998.
- [48] Puu G. and Gustafson I. Planar lipid bilayers on solid supports from liposomes—factors of importance for kinetics and stability. *Biochim. Biophys. Acta*, 1327:149–161, 1997.
- [49] Cha T. W., Guo A., and Zhu X. Y. Formation of supported phospholipid bilayers on molecular surfaces: Role of surface charge density and electrostatic interaction. *Biophys. J.*, 90:1270–1274, 2006.
- [50] Keller C. A., , Glasmästar K., Zhdanov V. P., and Kasemo B. Formation of supported membranes from vesicles. *Phys. Rev. Letters*, 84:5443–5446, 2000.
- [51] Jass J., Tjärnhage T., and Puu G. From liposomes to supported, planar bilayer structures on hydrophilic and hydrophobic surfaces: An atomic force microscopy study. *Biophys. J.*, 79:3153–3163, 2000.
- [52] Plant A. L. Supported hybrid bilayer membranes as rugged cell membrane mimics. *Langmuir*, 15:5128–5135, 1999.
- [53] Onclin S., Ravoo B. J., and Reinhoudt D. N. Engineering silicon oxide surfaces using self-assembled monolayers. *Angew. Chem. Int. Ed. Engl.*, 44:6282–6304, 2005.
- [54] Kunitake T. Synthetic bilayer membranes: Molecular design, self-organization, and application. *Angew. Chem. Int. Ed. Engl.*, 31:709–726, 1992.
- [55] Tang Z., Jing W., and Wang E. Self-assembled monolayer growth of phospholipids on hydrophobic surface toward mimetic biomembranes: Scanning probe microscopy study. *Langmuir*, 16:1696–1702, 2000.
- [56] Kalb E., Frey S., and Tamm L. K. Formation of supported planar bilayers by fusion of vesicles to supported phospholipid monolayers. *Biochim. Biophys. Acta*, 1103:307–316, 1992.
- [57] Waggoner A. S. and Stryer L. Fluorescent probes of biological membranes. *Proc. Nat. Acad. Sci.*, 67:579–589, 1970.
- [58] Easter J. H. DeToma R. P. and Brand L. Nanosecond time-resolved emission spectroscopy of a fluorescence probe adsorbed to l-alpha-agg lecithin vesicles. *Biophys. J.*, 16:571–583, 1976.

- [59] DeToma R. P., Easter J. H., and Brand L. Dynamic interactions of fluorescence probes with the solvent environment. *J. Am. Chem. Soc.*, 98: 5001–5007, 1976.
- [60] Easter J. H., DeToma R.P., and Brand L. Fluorescence measurements of environmental relaxation at the lipid-water interface region of bilayer membranes. *Biochim. Biophys. Acta*, 508:27–38, 1978.
- [61] Blatt E., Ghiggino K. P., and Sawyer W. H. A novel means of investigating the polarity gradient in the micelle sodium lauryl sulphate using a series of n-(9-anthroyloxy) fatty acids as fluorescent probes. *J. Chem. Soc. Faraday 1*, 77:2551–2558, 1981.
- [62] Sýkora J., Kapusta P., Fidler V., and Hof M. On what time scale does solvent relaxation in phospholipid bilayers happen? *Langmuir*, 18:571–574, 2002.
- [63] Zubrzycki I. Z., Yan X., Madrid M., and Tang P. Molecular dynamics simulations of a fully hydrated dimyristoylphosphatidylcholine membrane in liquid-crystalline phase. *J. Chem. Phys.*, 112:3437–3441, 2000.
- [64] Salah O. A. *Diss. Julius-Maximilian-University Würzburg*, 2001.
- [65] Hutterer R., Schneider F. W., Lanig H., and Hof M. Solvent relaxation behaviour of n-anthroyloxy fatty acids in pc-vesicles and paraffin oil: a time-resolved emission spectra study. *Biochim. Biophys. Acta*, 1323:195–207, 1997.
- [66] Dewar M. J. and Deminstan R. D. *II. Ampac 5.0 Semichem*, Shawnee: USA, 1994.
- [67] Acd/chemsketch freeware, version 10.00. *Advanced Chemistry Development, Inc., www.acdlabs.com*, pages Toronto, Canada, 2006.
- [68] Sumalekshmy S. and Gopidas K. R. Photoinduced intramolecular charge transfer in donor-acceptor substituted tetrahydropyrenes. *J. Phys. Chem. B*, 108:3705–3712, 2004.
- [69] Lahmani F., Breheret E., Zehnacker-Rentien A., Amatore C., and Jutand A. Intramolecular charge transfer properties in the excited state of paradisubstituted biaryls. *J. Photochem. Photobiol. A*, 70:39–49, 1993.
- [70] Lahmani F., Bréhéret E., Benoist d’Azy O., Zehnacker-Rentien, and Delouis J. F. Solvent effect on the excited state behaviour of donor-acceptor-substituted biaryls. *J. Photochem. Photobiol. A*, 89:191–199, 1995.

- [71] Jamroz D., Stangret J., and Lindgren J. An infrared spectroscopic study of the preferential solvation in water-acetonitrile mixtures. *J. Am. Chem. Soc.*, 115:6165–6168, 1993.
- [72] Wakisaka A., Takahashi S., and Nishi N. Preferential solvation controlled by clustering conditions of acetonitrile-water mixtures. *J. Chem. Soc. Faraday Trans.*, 91:4063–4069, 1995.
- [73] Braganza L. F. and Worcester D. L. Structural changes in lipid bilayers and biological membranes caused by hydrostatic pressure. *Biochem.*, 25: 7484–7488, 1986.
- [74] Marra J. and Israelachvili J. Direct measurements of forces between phosphatidylcholine and phosphatidylethanolamine bilayers in aqueous electrolyte solutions. *Biochemistry*, 24:4608–4618, 1985.
- [75] McArthur E. A., Ye T., Cross J. P., Petoud S., and Borguet E. Fluorescence detection of surface-bound intermediates produced from uv photoreactivity of alkylsiloxane sams. *J. Am. Chem. Soc.*, 126:2260–2261, 2004.
- [76] Nakashima N. and Kunitake T. Drastic fluorescence enhancement of cyanine dyes bound to synthetic bilayer membranes. its high sensitivity to the chemical structure and the physical state of the membrane. *J. Am. Chem. Soc.*, 104:4261–4262, 1982.
- [77] Lakowicz J. R. *Principles of Fluorescence Spectroscopy*, Plenum Pub. Corp., New York, 1999.
- [78] Using the Program PeakFit. SeaSolve Software Inc.:4.12 ed, 2003.
- [79] Rieber K., Sýkora J., Olzynska A., Jelinek R., Cevc G., and Hof M. The use of solvent relaxation technique to investigate headgroup hydration and protein binding of simple and mixed phosphatidylcholine/surfactant bilayer membranes. *Biochim. Biophys. Acta*, 1768:1050–1058, 2007.
- [80] Richert R. Spectral diffusion in liquids with fluctuating solvent responses: Dynamical heterogeneity and rate exchange. *J. Chem. Phys.*, 115:1429–1434, 2001.
- [81] Richert R. Theory of time dependent optical linewidths in supercooled liquids. *J. Chem. Phys.*, 114:7471–7476, 2001.
- [82] Wong A. K. Y. and Krull U. J. Surface characterization of 3-glycidoxypropyltrimethoxysilane films on silicon-based substrates. *Anal. Bioanal. Chem.*, 383:187–200, 2005.

- [83] Cras J. J., Rowe-Taitt C. A., Nivens D. A., and Ligler F. S. Comparison of chemical cleaning methods of glass in preparation for silanization. *Biosens. Bioelectron.*, 14:683–688, 1999.
- [84] Wang L., Wang L., Xia T., Bian G., Dong L., Tang Z., and Wang F. A highly sensitive assay for spectrofluorimetric determination of reduced glutathione using organic nano-probes. *Spectrochim. Acta A Mol. Biomol. Spectrosc.*, 61:2533–2538, 2005.
- [85] Tellinghuisen J., Goodwin P. M., Ambrose W. P., Martin J. C., and Keller R. A. Analysis of fluorescence lifetime data for single rhodamine molecules in flowing sample streams. *Anal. Chem.*, 66:64–72, 1994.
- [86] Castellana E. T. and Cremer P. S. Solid supported lipid bilayers: From biophysical studies to sensor design. *Surface Science Reports*, 61:429–444, 2006.
- [87] Cremer P. S. and Boxer S. G. Formation and spreading of lipid bilayers on planar glass supports. *J. Phys. Chem. B*, 103:2554–2559, 1999.
- [88] Holden M. A., Jung S. Y., Yang T., Castellana E. T., and Cremer P. S. Creating fluid and air-stable solid supported lipid bilayers. *J. Am. Chem. Soc.*, 126:6512–6513, 2004.
- [89] Schubert D. *Diss. Technische Hochschule Zürich*, 2006.
- [90] Parker C. A. *Photoluminescence of Solutions*, Elsevier:Amsterdam, 1968.
- [91] Meech S. R. and Phillips D. Photophysics of some common fluorescence standards. *J. Photochem.*, 23:193–217, 1983.
- [92] Beechen J. M., Gratton E., and Mantulin O. M. *GlobalsWE*, University of Florida:Irvine, 2007.
- [93] Lianos P. and Duportail G. Reactions in lipid vesicles. pyrene excimer formation in restricted geometries. effect of temperature and concentration. *Eur. Biophys. J.*, 21:29–34, 1992.
- [94] Horng M. L., Gardecki J. A., Papazyan A., and Maroncelli M. Subpicosecond measurements of polar solvation dynamics: Coumarin 153 revisited. *J. Phys. Chem.*, 99:17311–17337, 1995.